Title	The Environmental Measurement Using a Coherent White Light Continuum-Development of the White Light Depolarization Lidar System-
Author(s)	染川, 智弘
Citation	大阪大学, 2008, 博士論文
Version Type	VoR
URL	https://hdl.handle.net/11094/48748
rights	
Note	

The Environmental Measurement
Using a Coherent White Light Continuum

-Development of the White Light Depolarization Lidar System-

by

SOMEKAWA Toshihiro

Ph. D. Thesis

2008

Department of Earth and Space Science

Graduate School of Science, Osaka University

Abstract

Depolarization lidar (light detection and ranging) measurements were performed for the first time using a coherent white light continuum light ranging from UV to IR regions. Firstly, the polarization properties of the white light generated in a 9-m-long gas cell with krypton gas were investigated with a terawatt femtosecond laser system. The white light polarization is the same as that of the linearly polarized original laser. These results have a significant effect on the use of a white light depolarization lidar. The main characteristics of the white light depolarization lidar system are presented in chapter 2, along with a description of the depolarization measurements at 450 nm. The lidar system consisted of a depolarization channel at 450 nm and the five-wavelength Mie scattering channels at 350, 450, 550, 700, and 800 nm. This first observation provided the necessary foundation for the multi-wavelength depolarization lidar.

For further investigation in chapter 3, the white light depolarization lidar system was developed to permit simultaneous measurement of depolarization ratios at 450, 550, and 800 nm. The results presented here provided the wavelength dependence to enable the multi-wavelength depolarization ratio to be used as a method to evaluate the size of the atmospheric aerosols without using conventional inversion algorithms. Moreover, the T-matrix computation of depolarization ratio supports the idea that the particle size can contribute significantly to the depolarization ratio.

In chapter 4, an observation of Asian dust aerosols was described for the first time using the white light depolarization lidar system. Lidar depolarization ratios of 0.30-0.70 at 800 nm were obtained. These data revealed a higher depolarization ratio than usual (normally almost zero) in the lower troposphere. Thus, the white light lidar can identify Asian dust particles that pose a threat to cross-border pollution in Japan.

A method for evaluating the number density of particles in atmospheric clouds is presented, based on depolarization measurement of backscattering and multiple scattering from ice clouds. The lidar we used in the observation is a three-wavelength (450, 550, and 800 nm) depolarization lidar with a variable receiving field-of-view (FOV). The wavelength dependence of multiply scattered lidar returns has made possible the retrieval of cloud droplet size and the particle size density distribution.

White light lidar is an efficient tool for remotely measuring the multi-wavelength backscattered signal simultaneously, but the available wavelength is limited by the white light inten-

sity. In chapter 7, a noise reduction based on wavelet transform was proposed to detect the weak signals buried in noises. Firstly, the raw data are decomposed by means of the wavelet transform, secondly, the wavelet coefficients are shrunk, and finally, the denoised signal is reconstructed from the processed wavelet coefficients through the inverse wavelet transform. This method can improve quality of the lidar signal by reducing the noise without affecting the original signal. It also allows the detection of backscattered signals from clouds which were buried in noise. The result of this study demonstrated that wavelet signal denoising could improve the detectable range of the white light lidar system.

Last chapter summarizes the obtained results and present the future prospects of this field. This study shows that the white light lidar system can be utilized as sensor widely for meteorological and environmental measurement.

Table of contents

Chapter 7
Noise Reduction in White Light Lidar Signal
Based on Wavelet Transform 56

Chapter 8
Summary and Future Prospects 65

Acknowledgements

Chapter 1
Introduction

This chapter explains the basic characteristics of lidar techniques. Section 1.1 shows the applied geoscience significance of the lidar observation and lists the general lidar techniques. Section 1.2 focuses on basic theories on Mie scattering lidar, which plays an essential role in lidar measurement. Section 1.3 illustrates a coherent white light continuum. It shows the principle of the coherent white light continuum. Section 1.4 outlines this thesis.

1.1. Introduction to lidar

1.1.1. Lidar and monitoring of the atmosphere

LIDAR (light detection and ranging) is a widely used tool for the remote sensing of the atmosphere using laser. Lidar techniques have high spatial and temporal resolution, the possibility of observing the atmosphere at ambient conditions, and the potential of covering the height range from the ground to more than 100 km altitude. These make them very powerful and attractive techniques for monitoring the atmosphere, especially in recent times when global environmental problems have become very important. The variety of interaction processes of the emitted radiation with the atmospheric constituents allow the determination of the basic atmospheric variable state such as temperature, pressure, humidity, and wind, as well as the measurement of trace gases, aerosols, and clouds (Weitkamp, 2005).

Lidar systems are laser-based systems that operate on principles similar to that of conventional radar (radio detection and ranging). Although microwave radar has certain advantage, it is limited by its longer wavelength to accurately characterize small particles such as atoms, molecules, and aerosols. However, lidar has adequate resolution for these small particles because of its shorter wavelength. Therefore, lidar has been used to investigate the complex dynamic system of the atmosphere during the industrial age, including the destruction of the ozone layer (Browell et al., 1990) and the global warming (Tegen et al., 1996). Lidar helps monitor the intercontinental transport of air pollution such as volcanic ash, photochemical smog, Asian dust (Shimizu et al., 2004), and forest-fire smoke. Lidar instruments can operate from the ground, aircraft, or the Space Shuttle. In the near future satellite-based lidar instruments will carry out global observations of atmospheric constituents from space.

1.1.2. Conventional lidar techniques

Lidar can be classified with respect to the variety of interaction process of the emitted radiation with the atmospheric constituents. Table 1-1 summarizes the lidar applications in observation of the atmosphere. Elastic-backscatter lidar is the classic form of lidar and has in principle been described in the next section. Rayleigh and Mie scattering are elastic scattering in which the wavelength of the scattered light is the same as that of the incident light to the target. Rayleigh scattering can be defined as the elastic scattering from particles that are very small compared to the wavelength of the scattered radiation. In the context of lidar, Rayleigh scattering is always used as a synonym for molecular scattering from nitrogen and oxygen. Mie scattering lidar is used to detect the clouds and aerosols with size comparable to the wavelength of the radiation, or larger. In the region where particle's radius and wavelength are of similar magnitude, the wavelength dependence of the scattering intensity varies strongly. Wavelength-dependent detection of light scattering can therefore be used to obtain information on size and other parameters of atmospheric aerosol particles in the radius range from about 50 nm to a few micrometers.

The Raman lidar technique makes use of an inelastic scattering process which involved the change of the vibrational-rotational energy level of the molecule. The frequency shifts of scattered radiation are characteristic of the interacting molecule. In absorption methods, two laser beams, one with a wavelength corresponding to a strongly absorbing transition and one with a wavelength at which there is only weak absorption, are transmitted into atmosphere. From the difference between the two signals, the density distribution of the absorbing species can be determined. Resonance fluorescence is obtained if the energy of the incoming photon

coincides with the energy of a transition in an atom, ion, or molecule from one level into another level.

In all of the above method, the intensity of the backscattered signals is the only important quantity. In Doppler lidar, the wind speed can be determined from the Doppler shift of the scattered light. Polarization lidar is utilized to estimate the shape of the scattering particles and the degree of multiple scattering from the depolarization ratio.

Table 1-1. Lidar methods.

Type of interaction	Measured species
Mie scattering	aerosols, clouds, smog, mist
Rayleigh scattering	atmospheric molecules (N_2, O_2)
Raman scattering	N_2, O_2, H_2O, NO_2, SO_2, etc.
Resonance absorption	H_2O, O_3, NO_2, SO_2, etc.
Resonance fluorescence lidar	Na, Fe^+, etc.

Property of light	Measured quantity
Polarization	shape
Doppler shift	wind speed

1.1.3. White light lidar

After the chirped pulse amplification technique was invented in the mid-1980s, tabletop short pulse laser systems became popular in many scientific fields. The development of this short pulsed laser sources with high peak powers has resulted lots of interest in the area of the extreme nonlinear phenomenon. The propagation of high-intensity ultrashort pulses in transparent nonlinear medium gives strong nonlinear effects such as self-focusing, self-phase modulation, and so on, which lead to strong modifications of the pulse characteristics (Shen, 1984; Close et al., 1966; Ranka et al., 1996; Brodeur and Chin, 1998; Nishioka et al., 1995; Kasparian et al., 2000).

One of the most interesting features observed is the formation of the coherent white light continuum whose wavelength ranges from the UV to the IR region. This phenomenon has been observed in a variety of transparent materials including gases, liquids, and solids. Because the white light pulse has spatial and frequency coherence, the energy can be concentrated in a small

space and a short time like the original laser. The full-angle divergence generated in rare gases was about 1 mrad. Thus, applications of this white light have spread widely to include femtosecond time-resolved spectroscopy (Klimmov and McBranch, 1998; Kovalenko et al., 1999; Wang et al., 1994), broadband spectrum lidar (Rairoux et al., 2000, Galvez et al., 2002, Kasparian et al., 2003), and so on.

In 2000, Rairoux (2000) reported the application of this novel light source for atmospheric remote sensing. The white light continuum was generated by focusing a high-power femtosecond laser pulses (220 mJ, 100fs) using 30-m focal length or not focusing at all into atmosphere. They demonstrated that the remote generation of a white light source not only allows spectrally integrated measurement of the backscatter signal from clouds up to 12 km high, but also represents a new way to access the range-resolved multi-trace gas analysis in the atmosphere by performing measurements of the oxygen molecule and water vapor.

The fundamental aspects of the observed nonlinear optical phenomena and their potential application for optical remote sensing provide the basis for a large-frame French-German project called TERAMOBILE (for "Terawatt laser in a mobile system") (Kasparian et al., 2003). The femtosecond lidar system was installed in a mobile container laboratory, so it had the advantage of moving to different and relevant sites easily. Teramobile has been constructed to study on three themes, fs filament-based lightning control, the propagation of ultrashort laser pulses in air (Mechain et al., 2005; Mejean et al., 2005), and new possibilities of sounding the atmosphere (Mejean et al., 2004; Boutou et al., 2005).

In Japan, the white light lidar project has been started by Institute for Laser Technology (ILT) since 2000 (Galvez et al., 2002). The project presently involves three research institutes, Osaka University, ILT, and De La Salle University. Contrary to white light lidar experiments in Teramobile projects, our experiment was based on white light generated in Kr gas (Nishioka et al., 1995). Therefore, the light source can be characterized directly by observations from the ground, which allowed us to construct a white light depolarization lidar (Somekawa et al., 2006).

1.2. Principles of Mie backscattering lidar

1.2.1. Lidar setup

A typical Mie backscattering lidar arrangement is shown in Fig. 1-1. Light pulses are

transmitted to the atmosphere, where they are attenuated and scattered. The backscattered light is collected by a telescope, usually placed coaxially with the laser emitter, and then detected by a sensitive photomultiplier. The backscattered signal contains information about the components present in the atmosphere. Because the light takes longer to return to the receiver from targets located farther away, the time delay of the return is converted into distance. Since a pulsed laser is used, the intensity of the backscattered light can be recorded as a function of time, and thus provide the required spatial resolution of the measurement.
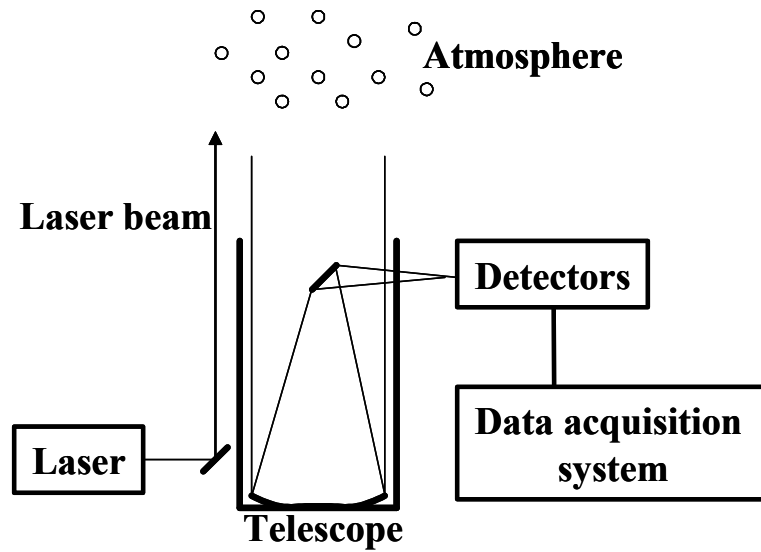
Fig.1-1. Concept of Mie scattering lidar method.

1.2.2. Lidar equation

The received signal from a lidar system can be expressed generally by the lidar equation (Fernald, 1984; Sasano and Browell, 1989);

$$V(\lambda,z) = K(\lambda,z)\frac{\beta_1(\lambda,z) + \beta_2(\lambda,z)}{z^2}\exp\left\{-2\int_0^z[\alpha_1(\lambda,z') + \alpha_2(\lambda,z')]dz'\right\}, \quad (1\text{-}1)$$

$V(z)$ is the received signal for range z, $K(\lambda)$ is the system constant, which depends on the different lidar system parameters, β_1 and β_2 are the aerosol and air molecular volume backscatter coefficients, respectively; α_1 and α_2 are the aerosol and air molecular volume extinction coefficients, respectively. However, this lidar equation contains two unknown parameters, backscatter and extinction coefficients, and cannot be solved. Therefore, assuming a relationship between the two parameters, these parameters are determined for various measurement conditions.

The extinction/backscatter ratios are defined as follows:

$$S_1 = \frac{\alpha_1}{\beta_1} \text{ for aerosols (subscript 1),} \tag{1-2}$$

$$S_2 = \frac{\alpha_2}{\beta_2} \text{ for air molecules (subscript 2),} \tag{1-3}$$

where S_2 is a constant for air molecules, $S_2 = \frac{8\pi}{3}$, and at a specific wavelength S_1 is a variable dependent on the characteristics of aerosols. Typical values of the S_1 parameter are 50 sr and 20 sr for aerosol and cloud, respectively.

According to Fernald (1984), the solution for the lidar equation can be obtained from Eqs. (1-1)-(1-3), that is,

$$\beta_1(\lambda, z) = -\beta_2(\lambda, z) + \frac{X(z)\exp\left[2(S_1 - S_2)\right]\int_z^{z_C}\beta_2(\lambda, z')dz'}{A + 2S_1\int_z^{z_C}X(z')\exp\left[2(S_1 - S_2)\right]\int_z^{z_C}\beta_2(\lambda, z'')dz''}, \tag{1-4}$$

where $A = \frac{X(z_C)}{\beta_1(z_C) + \beta_2(z_C)}$, z_C is the calibration height ($z_C > z$), $X(z) = V(z)z^2$ is the range normalized signal. At the calibration height, z_c, it was assumed that the backscattering coefficient of clouds and/or aerosol is negligible. However the backscatter coefficients by aerosols, β_2, must be determined by meteorological measurements assuming appropriate scattering coefficients by atmospheric molecules.

1.2.3. Molecular component of the backscattered signal

Since the size of air molecules is very small compared to lidar wavelengths used in our observations, elastic backscattering by atmospheric gases is described by the Rayleigh scattering approximation. The molecular volume backscattering coefficient, $\beta_2(\lambda, z)$, is obtained from

$$\beta_2(\lambda, z) = N(z)\left(5.45\left(\frac{550}{\lambda[\text{nm}]}\right)^4\right) \times 10^{-32}\left[\text{m}^2\text{sr}^{-1}\right], \tag{1-5}$$

where λ is the wavelength of the return signal in nm, $N(z)$ is the number density with altitude z (Collis and Russell, 1976).

The number density is derived through the expression

$$N(z) = \frac{\rho(z) \times N_A}{M_d} \quad , \tag{1-6}$$

where $\rho(z)$ is the air density, N_A is Avogadro number $= 6.0247 \times 10^{23}$, and M_d is molecular weight of air $= 28.97$ g/mol. The air density is derived from the equation of state of the moist air

$$\rho(z) = \frac{p - e}{R_d T} + \frac{e}{R_v T} \quad , \tag{1-7}$$

where p denotes the pressure of moist air, e is the partial pressure of water vapor in moist air, R_d is the specific gas constant for dry air, and R_v is the specific gas constant for water vapor.

$$\rho(z) = \frac{p}{R_d T} \left(1 - (1 - \varepsilon) \frac{e}{p} \right) \tag{1-8}$$

with $\varepsilon = M_v / M_d = 0.622$, where M_v is molecular weight of water vapor $= 18.015$ g/mol.

$$\rho(z) = \frac{p}{R_d} \left(\frac{1}{T} - \frac{0.38}{T'} \right), \tag{1-9}$$

where p is in dyn/cm^2, T' is the dew point in Kelvin, and $R_d = 2.87 \times 10^6$ erg/gK. (P(hPa) $=$ P$\times 10^3$ dyn/cm^2)

Pressure, temperature, and dew point at various altitudes are from the Radiosonde at Shionomisaki station (33.27°N, 135.46°E) which is about 153 km south of the Lidar site. The radiosonde data gather data at random altitudes. To obtain the molecular volume backscattering coefficient that has the same altitudes as the raw lidar data, a collinear approximation using the method of least squares was performed.

1.2.4. Angstrom coefficient

The size distribution of particles can be estimated from the wavelength dependence of backscattering coefficient given by $\beta_1(\lambda_2) = \beta_1(\lambda_1)(\lambda_1/\lambda_2)^{\mathring{a}}$. Then

$$\mathring{a} = -\ln\{\beta_1(\lambda_1)/\beta_1(\lambda_2)\}/\ln(\lambda_1/\lambda_2) \qquad (1\text{-}10)$$

where λ_1 and λ_2 are wavelength, $\mathring{a}$ is the wavelength exponent or the angstrom coefficient. If the aerosol number distribution is represented in a certain size range by a relation of the form

$$\frac{dN}{dD_p} \approx D_p^{-\nu} \qquad (1\text{-}11)$$

then $\mathring{a} = \nu - 3$. Higher values of $\mathring{a}$ indicate small particles whereas smaller values, sometimes zero or negative values which are usually obtained for clouds, indicate large size particles.

1.3. Generation of ultra-short white light continuum

When electric field E is applied to a medium, birefringence effect called "electro-optics effect" occurs. The case where the induced refractive index is proportional to square of electric field E, it is called "Kerr effect". An intense electric field of light causes "optical Kerr effect". Every material has a nonlinear refractive index, so the response for electric field E is expressed as follows,

$$n = n_0 + n_2 E^2 , \qquad (1\text{-}12)$$

where n_0 is the refractive index and n_2 is the nonlinear refractive index. In a material with the refractive index that increases with intensity, the change of the nonlinear refractive index causes the self-trapping and self-phase-modulation phenomenon in the intense laser beam propagation.

1.3.1. Self-trapping

When the refractive index of a medium changes with intensity of light, the phase velocity will change with beam intensity. Upon entering the medium with a nonlinear refractive index, a portion of high intensity differs in a refractive index from a portion of low intensity. For exam-

ple, in a substance that the nonlinear refractive index is positive, the central part of the beam having a higher intensity should experience a larger refractive index than the edge. Therefore, the central part of the beam travels at a slower velocity than the edge. Consequently, the wave surface curves as seen in Fig. 1-3.

wave surface

nonlinear refractive index (n_2) > 0

Gaussian pulse shape
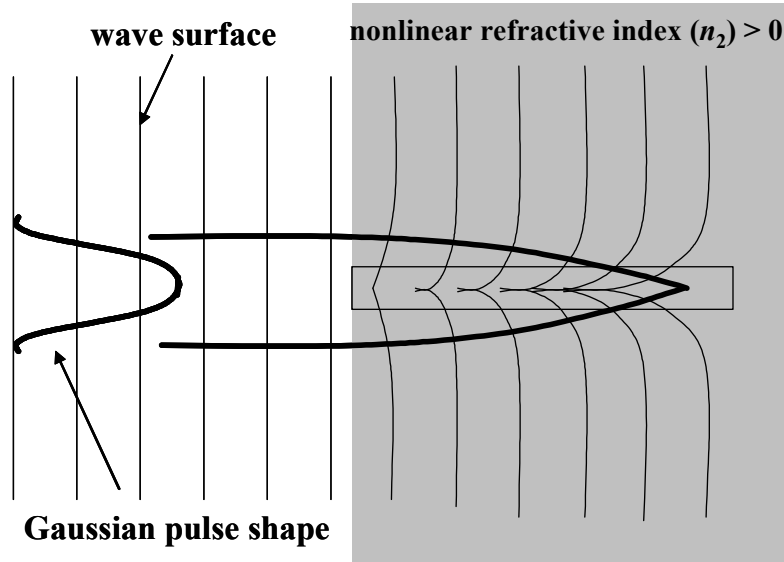
Fig. 1-3. Distortion of the wavefront of a laser beam leading to self-focusing in a nonlinear medium.

The self-trapping of a femtosecond and high intensity light pulse produced critical balancing of the self-focusing and diffraction. The spatial phase delay due to the nonlinear refractive index n_2 is given by the *B*-integral factor,

$$B \equiv \frac{2\pi}{\lambda} \int_0^L n_2 I(z) dz$$

, (1-13)

where L is the interaction length, λ is the laser beam wavelength, $I(z)$ is the light intensity. On the other hand, when the divergence is based on the diffraction, the Guoy Phase Shift φ for range z is given by

$$\varphi = \tan^{-1} \frac{z}{z_R} \approx \frac{z}{z_R} \quad (z < z_R),$$

(1-14)

where z_R is the Rayleigh length and there are the following relations to the Gaussian beam radius w_0 :

9

$$z_R = \frac{\pi w_0^2}{\lambda} .$$

(1-15)

In a convergent beam, power of the self-focusing always exceeds that of the diffraction, the convergent beam keep up the self-focusing until when fatal break down is produced. For self-trapping, it is required to produce a balance of the self-focusing and diffraction. The progress in the phase based on the diffraction at the center of a laser beam is $\varphi = \pi/4$ for $z = z_R$. To keep beam balance, the self-phase-modulation B is necessary to be $\pi/4$ for $z = z_R$. The Gaussian beam radius satisfied this self-trapping condition is given by

$$w_{0,sf} = \frac{\lambda}{\sqrt{8\pi n_2 I}} .$$

(1-16)

The beam diameter of self-focusing is proportion to the wavelength and is inversely proportion to square root of the light intensity. The threshold power that causes self-focusing is given by

$$P_{0,sf} = \pi w_{0,sf}^2 I = \frac{\lambda^2}{8n_2} ,$$

(1-17)

which depends on wavelength and the nonlinear refractive index. The nonlinear refractive index of gas media is listed in Table 1-2 (Nishioka et al., 1995). The power that was needed to balance diffraction were calculated to be $\sim$10 GW and $\sim$3.2 GW in N_2 and Kr, respectively ($\lambda = 800$ nm).

Table 1-2. Nonlinear refractive index for various gases.

Gas	n_0	$n_2(\times 10^{-20}\text{cm}^2/\text{W})$
N_2	1.000297	8.18
Ne	1.000069	0.716
Ar	1.0002837	9.12
Kr	1.000427	24.9
Xe	1.000702	73.2

1.3.2. Self-phase-modulation (SPM)

Another effect of the nonlinear refractive index is the self-phase-modulation (SPM). The phase delay causes the decreasing of the instantaneous frequency as the light intensity increase at the rising part of laser pulses and instantaneous frequency decreases as the light intensity decreases at the decay part of laser pulses as shown in Fig. 1-4.

The temporal variation of refractive index $\Delta n(t)$ is described as a function of light intensity $I(t)$,

$$\Delta n(t) = n_2 E^2 = n_2 \sqrt{\frac{\mu_0}{n_0^2 \varepsilon_0} I(t)}$$

$$\text{(1-18)}$$

When the laser beam of wavelength λ propagates the medium of length L, the change of the frequency $\Delta \omega(t)$ is a time variation of phase difference $\Delta \varphi(t)$. Thus, the frequency broadening is shown in the following equation,

$$\Delta \omega(t) = -\frac{\partial}{\partial t} \Delta \phi(t) = \frac{2\pi n_2 L}{\lambda} \frac{\partial}{\partial t} |E(t)|^2 = \frac{2\pi n_2 L}{\lambda} \frac{\partial}{\partial t} I(t) \sqrt{\frac{\mu_0}{n_0^2 \varepsilon_0}}$$

$$\text{(1-19)}$$
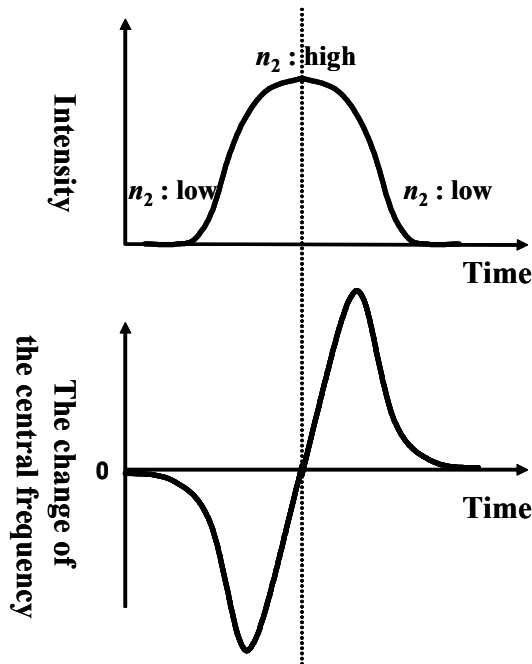
Fig. 1-4. Self-phase-modulation (SPM).

11

1.3.3. White light generated in rare gas

Spectral distributions of the continuum produced in rare gases are shown in Fig. 1-5 (Nishioka et al., 1995). An intense continuum from IR to near UV was observed in Xe, Kr, and Ar. However, the continuum in Ne, which has a small nonlinear refractive index, shows the conventional spectrum shape which is produced by the non-trapped laser beam. This is because the spectral intensity in the visible region was dependent on the nonlinear refractive index (Nonlinearity: Xe > Kr > Ar > Ne). If the nonlinear refractive index is large, the self-focusing is strong and the light intensity of the self-trapping channel is high. Simultaneously, ionization energy (Ionization Energy: Xe < Kr < Ar <Ne) is small, then multi-photon absorption is easy to occur. Consequently, the cutoff point of the plateau and the spectral intensity change inversely in the visible region. Since rare gases are used, there are no vibration and rotation absorption and it is completely transparent for a far-infrared region. Moreover, the loss of stimulated Raman scattering is not produced. Because of this rare gases were useful nonlinear medium. Thus, in view of the above reasons, the best choice is the use of Kr gas as nonlinear media since Kr gas give high intensity visible and near UV regions used in this lidar experiment.

Fig. 1-5. The White Light Spectrum from Rare Gas Cell measured by Nishioka et al. (1995).

Spectral intensity of the hyper-continua generated in atmospheric pressure rare gases.

The laser wavelength and laser power are 790 nm and 1.6 TW, respectively.

1.4. Scope of this thesis

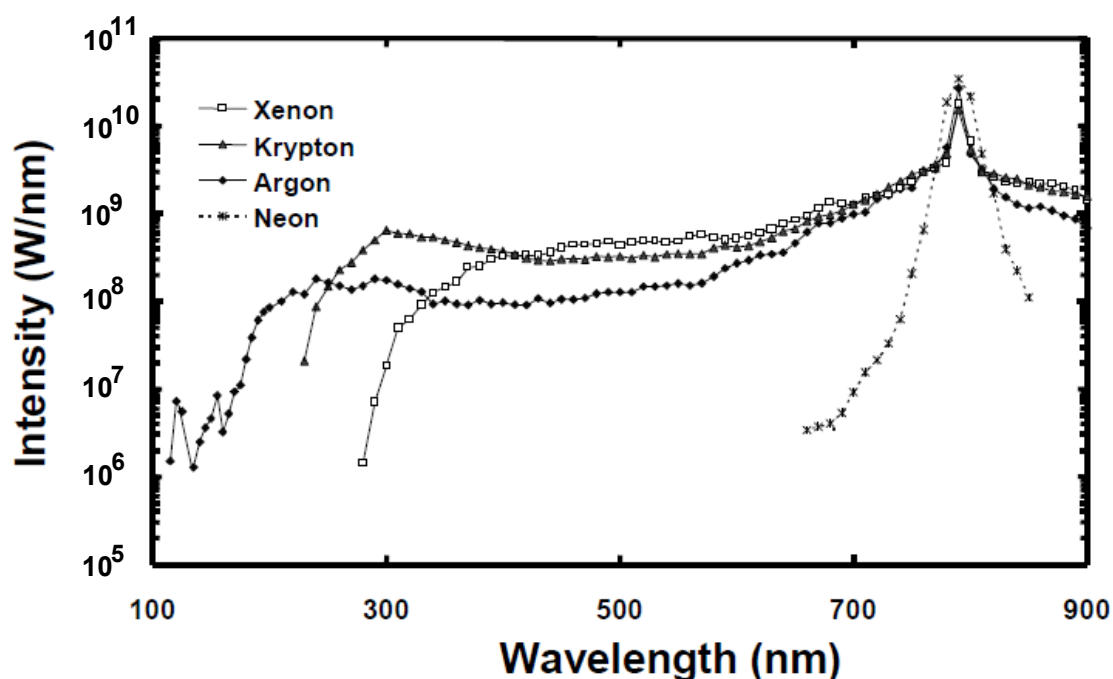The purpose of this thesis is to develop a new environmental measurement method using the coherent white light continuum. The coherent white light continuum is a novel and attractive laser source with a broadband spectrum, a linear polarization, and an ultra-short pulse. Therefore, the combined use of the multi-wavelength simultaneous measurements and the depolarization technique was performed after building the white light lidar system in this thesis. This study provides the basis for extending the range of applications such as the monitoring of greenhouse gases or the remote detection of biological agents being used as weapons (Fujii et al., 2006).

The work presented in this thesis is organized as follows. A short introduction to lidar is given in chapter 1. This chapter also presents the basic principles of the Mie backscattering lidar and the coherent white light continuum. After that, the instrumentation of the new white light depolarization lidar is given in chapter 2. The polarization properties of the white light continuum and the first observation results are discussed. In chapter 3, examples from the data obtained with the new simultaneous 3-wavelength depolarization lidar are given. This chapter gives a more detailed description of the depolarization measurements and also shows the evaluations of particle size and shape from the measured depolarization ratio using the conventional Angstrom coefficients and T-matrix simulations. A more detailed description of the T-matrix computations is given in chapter 6. As an environmental measurement example from the white light lidar the chapter 4 shows the Asian dust profiles obtained by the white light depolarization system. Future studies for white light lidar are discussed on chapters 5 and 7. These are the depolarization measurements of multiple FOV on chapter 5 and on chapter 7 the noise reduction based on the wavelet transform was proposed. Last chapter summarizes the obtained results and present the prospects of this field for future white light lidar.

Chapter 2
Depolarization Lidar
Using a White Light Lidar System

This and the succeeding chapters describe examples of practical observations to which the white light lidar technologies described in previous chapter are applied. Chapter 2 introduces some examples of depolarization lidar in tropospheric atmosphere using the coherent white light continuum. The initial experiments used the depolarization lidar method, and were intended to provide a proof-of-principle that the white light depolarization lidar works, and that results correspond with more traditional measurement techniques.

2.1. Introduction

Elastic backscatter lidar is perhaps the most widespread and robust kind of lidar capable of providing profiles of cloud and aerosol structures within the atmosphere. The addition of polarization detection provides information about the phase of cloud particles and the type of aerosol particles. These techniques rely on the basic assumption that nonspherical particles depolarize the backscattered light, whereas spherical particles do not.

Such a comparison employ the linear depolarization ratio δ ($=S/P$) defined as the ratio of the perpendicular signal (S-polarization) to the parallel signal (P-polarization). Sassen (1990) provides an overview of different cloud types and their corresponding δ values (Table 2-1). For

example, spherical water droplets produce no depolarization ($\delta \sim 0.0$), ice crystals and snowflakes can produce $\delta \sim 0.5$, and rimed ice and particles with complex surfaces have $\delta > 0.6$.

Table 2-1. Key for identifying the ranges of depolarization ratios δ (from Sassen et al., 1990).

δ	Interpretation
≤ 0.15	Liquid cloud
0.16-0.25	Liquid-dominated, some ice likely
0.26-0.35	Mixed-phase conditions
0.36-0.45	Typical ice cloud
0.46-0.55	Complex ice crystals or aggregates
0.56-0.65	Moderate-to-heavily rimed ice particles
> 0.65	Graupel particles

In general, this assumption is valid only when the signal is dominated by single scattering. When significant multiple scattering is present, even spherical particles generate depolarized signal, thus mistaking multiple-scattering-induced depolarization for particle-shape-induced depolarization (Pal and Carswell, 1973). Furthermore, theoretical studies showed that particles with small dimensions compared with the wavelength of the lidar do not show depolarization even if they are nonspherical (Toon et al., 1990; Mishchenko and Sassen, 1998; Murayama et al., 1999). As a result, the discrimination between spherical and nonspherical particles was restricted to a coarse classification. Therefore, additional lidar observations such as the multi-wavelength depolarization lidar (Stefanutti et al., 1992) and the combined use of the depolarization technique and other lidar techniques such as Mie scattering lidar and Raman lidar (Althausen et al., 2000) should be performed. However, it is troublesome to increase the number of light sources due to difficulties in the alignment of the transmission system.

The development of the terawatt femtosecond laser system has resulted in considerable interest in the area of extreme nonlinear phenomenon. One of the most interesting features observed is the formation of the coherent white light continuum whose wavelength ranges from the UV to the IR region (Nishioka et al., 1995; Kasparian et al., 2000). This "white light" lidar (Rairoux et al., 2000; Galvez et al., 2002; Kasparian et al., 2003) has an advantage in simultaneous and multi-wavelength measurements for several atmospheric species. Also, the white light is preferentially scattered in the backward direction, which enhances the lidar signal (Yu et al., 2001). These results have strong implications for lidar applications of the white light continuum.

In this chapter, we report whether the coherent white light continuum can be used for depolarization measurement in the same way as the conventional lidar. The white light continuum generated in Kr gas contains the high intensity wavelength region that is used in this lidar system and can be characterized by the ground-based experiments. The present lidar system was derived from a previous model (Galvez et al., 2002) and has been implemented with the new wavelengths. The system now operates at 350, 450, 550, 700, and 800 nm. In addition, depolarization measurements can be performed at the 450 nm channel. The research reported in this chapter describes the first use, as far as we know, of the coherent white light continuum for the depolarization remote sensing.
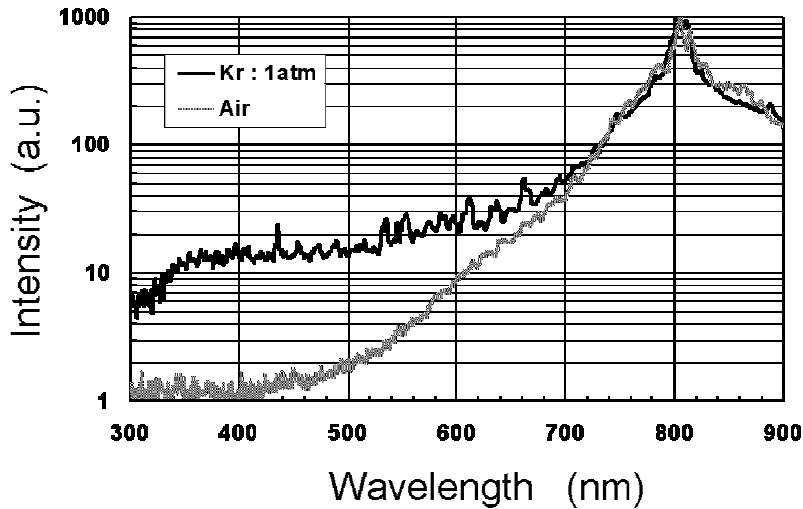
Fig. 2-1. White light spectra converted in the Kr gas cell (upper) and air (lower).

2.2. Experimental setup

2.2.1 Laser system

The femtosecond laser system consists of a Ti:sapphire oscillator and a CPA amplification chain. The laser transmitter consists of a tabletop terawatt Ti:sapphire laser system which operates at 800 nm. It has a front end, which is a combination of a Ti:sapphire oscillator pumped by a laser diode (LD)-pumped green Nd:YVO4 CW-laser and a regenerative amplifier pumped by a LD-pumped green Nd:YLF laser operated at 1 kHz. The output of the front end is a 100 fs pulse with an energy of 0.8 mJ. The uncompressed front-end pulse is introduced into a multipass Ti:sapphire amplifier which is pumped by two frequency-doubled Nd:YAG lasers. The final output energy is 100 mJ with a pulsewidth of 100 fs and a repetition rate of 10 Hz. To generate

the white light, output from the Ti:sapphire laser system is focused by a lens with a focal length of 5 m into a 9-m-long traveling tube filled with krypton gas. Figure 2-1 shows the white light spectra generated in Kr gas as the nonlinear materials, as compared to the case in air.

2.2.2. Polarization properties of a coherent white light continuum generated in Kr gas

It is essential that the transmitted beam keeps the linear polarization for the depolarization lidar. The polarization of the generated white light continuum is believed to be the same as the input laser polarization (Srivastava and Goswami, 2003). However, it has been reported that the polarization properties depend on the medium in which the white light continuum is generated (Midorikawa et al., 2002). Hence, the generated white light continuum should be characterized before the lidar applications. In this experiment, the white light continuum was generated at ground level in a 9-m-long gas cell with krypton gas as a nonlinear medium.

The polarization of the white light continuum was measured using a Wollaston polarizing Prism with an effective range of 350-2300 nm. A $\lambda/2$ plate and a band-pass filter were inserted before the Wollaston Prism to confirm the liner polarization of the laser at 450 nm and 800 nm. The polarization of the white light generated in Kr gas was changed by rotating the angle of the $\lambda/2$ plate. Each output signal from a Si-PIN photodiode (M5210, Matsusada Precision Inc.) was accumulated using a digital oscilloscope. The data were measured by taking the average of 50 signals to reduce the effects of beam intensity fluctuation.

The original P and S (intensity vs. rotation angle) curves in Fig. 2-2 show the linear polarization of the original laser without the focusing lens and Kr gas cell. It is evident from the 450 nm and 800 nm curves in Fig. 2-2 that the generated white light is linearly polarized. Also, a $\lambda/2$ plate and a polarizer (λ = 670 - 930 nm, T_P>99 %, R_S>80 %) were oriented to maximize the P-polarization of the incident laser before it reaches the Kr gas cell. As shown in Table 2-2, the output white light is strongly polarized in the P-polarization direction. The direction of the white light polarization generated in the Kr gas cell is the same as that of the original laser. These experiments demonstrated the potentialities of this polarized white light continuum as a light source in depolarization lidar.
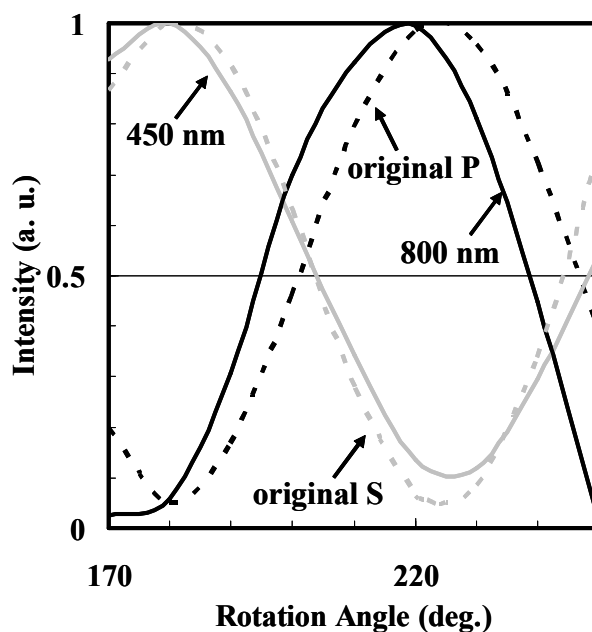
Fig. 2-2. Rotation angle dependence of original laser
and the white light through the Wollaston prism.

Table 2-2. The polarization characteristic in wavelength.

white light	$\dfrac{P-S}{P+S}$
800 nm	0.999
700 nm	0.995
550 nm	0.962
450 nm	0.960

2.2.3. Lidar experiment

The lidar system used in the present investigation has been designed to permit depolariza-
tion measurements. Backscattering light is collected by a 30-cm diameter Newtonian telescope
and is then collimated by a lens. The light passes along a light guide consisting of a pair of star-
diagonal prisms and is then directed to a 6-channel simultaneous measurement system. As
shown in Fig. 2-3, the light is separated into six channels using dichroic mirrors and a cold mir-
ror. The detection unit is aligned by means of a He-Ne laser and a halogen lamp. Narrow
band-pass filters, each having a 40-nm bandwidth, and with center wavelengths at 350, 550, 700,
and 800 nm, respectively, are placed in front of the photomultipliers to spectrally resolve the
backscattered light. For the 450 nm, an interference filter with a 457.9-nm center wavelength

and a 10-nm bandwidth is used. Each output signal from the photomultipliers is accumulated using a digital oscilloscope triggered by a common pulse signal synchronizing to the laser emission at 10 Hz. A rotatable $\lambda/2$ plate is placed between the 450-nm interference filter and the beamsplitter cube to line up the polarization axis of the beamsplitter cube with the polarization vector of the transmitted white light. This is done by directing a strongly attenuated white light on to the telescope and to the 6-channel receiving system using two mirrors. The $\lambda/2$ plate is rotated until the S-polarization channel is zero and the P-polarization channel is at the maximum.

DM: Dichroic Mirror, **M**: Mirror, **PM**: Photomultiplier,
BPF: Bandpass Filter, **CLDM**: Cold Mirror, **BM**: Beamsplitter
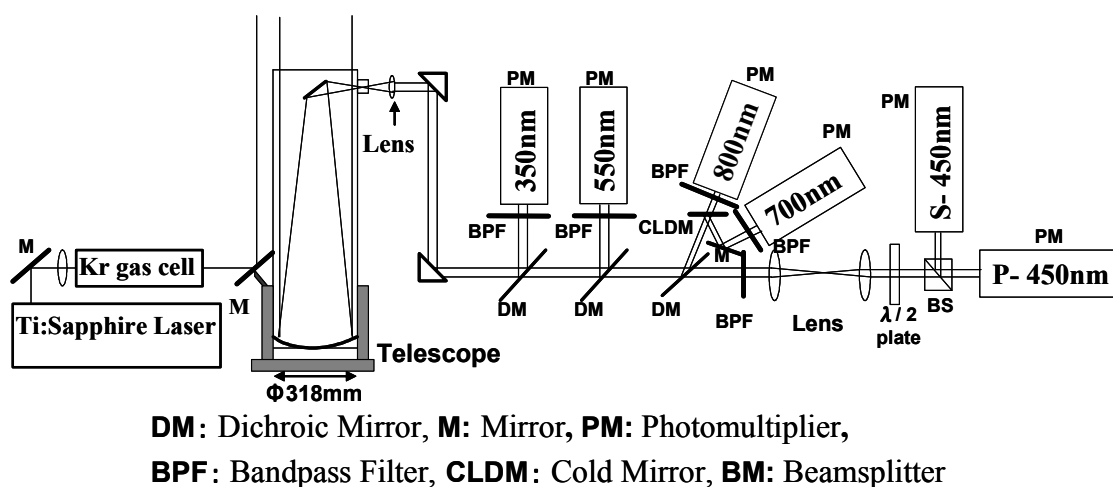
Fig. 2-3. Schematic diagram of the six-channel simultaneous measurement system.

2.3. Results and discussion

Lidar measurement was carried out on March 23, 2005 at Suita, Osaka. The optical power measured by lidar depends on the backscattering light by clouds and aerosols present in the atmosphere. Since the light takes longer to return to the receiver from targets located farther away, the time delay of the return is converted into distance (height). The received signal from a lidar system is corrected as

$$\text{range squared corrected signal} = (S - S_0)R^2,$$

where S is signal intensity, S_0 is the background signal, and R is the range between the laser source and targets.

Figure 2-4 shows an example of 30-minutes period, range squared corrected simultaneous backscattering profiles at 350, 450, 550, 700, and 800 nm wavelengths. Each profile was an av-

erage of consecutive 500 shots in 1 minute. Backscattering peaks corresponding to 0.6 km and 1.0 km in height were caused by running clouds and observed in all channels.

Fig. 2-4. Simultaneous measurements of the range squared corrected backscattered signal from atmosphere (2005/03/23 1:53~2:22 AM).

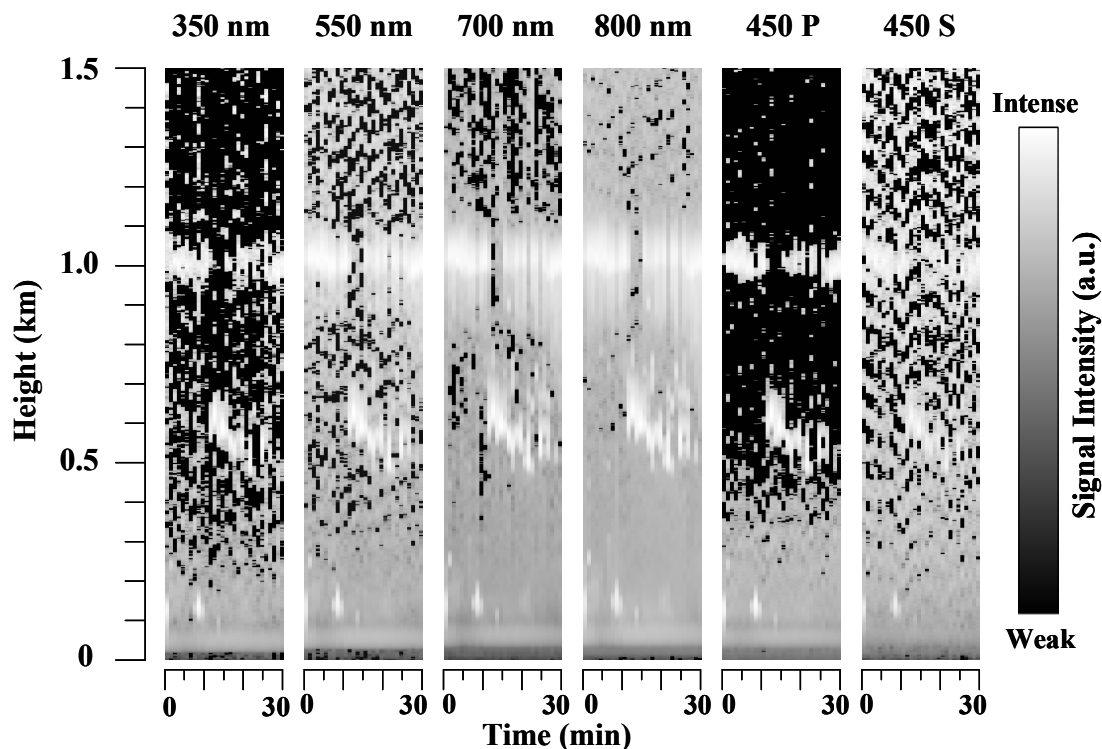Figure 2-5 shows sample displays of the backscattered signals from clouds at 450 nm. In Fig. 2-5, higher depolarization ratios were observed in the cloud layer. In Fig. 2-5(b) it is observed that the S-polarization signal peak is shifted upward with respect to the P-polarization signal due to multiple-scattering (Pal and Carswell, 1973). The observed values of δ were, respectively, 0.63 and 0.58 in Figs. 2-5(a) and 2-5(b), indicating relatively high value for not so much water droplet clouds but ice clouds (Sassen et al., 1990). Also, a value of 0.22 for δ in Fig. 2-5(c) may indicate a mixed phase cloud (Sassen et al., 1990). We obtained the radiosonde data at close time to our lidar measurements (21:00, 22 March 2005 and 9:00, 23 March 2005) at Shionomisaki station (33.27 N, 135.46 E), which is about 153 km south of the lidar site, are plotted in Fig. 2-6 as a reference. These meteorological data were provided by Japan Meteorological Agency. The temperatures at 0.6 km and 1.0 km were between 10 to 15 degrees Celsius, which is not as cold as the temperature regime in which ice clouds usually dominate. In these lidar measurements, we observed the high δ value as compared with the conventional depolarization lidar (Sassen et al., 1990).
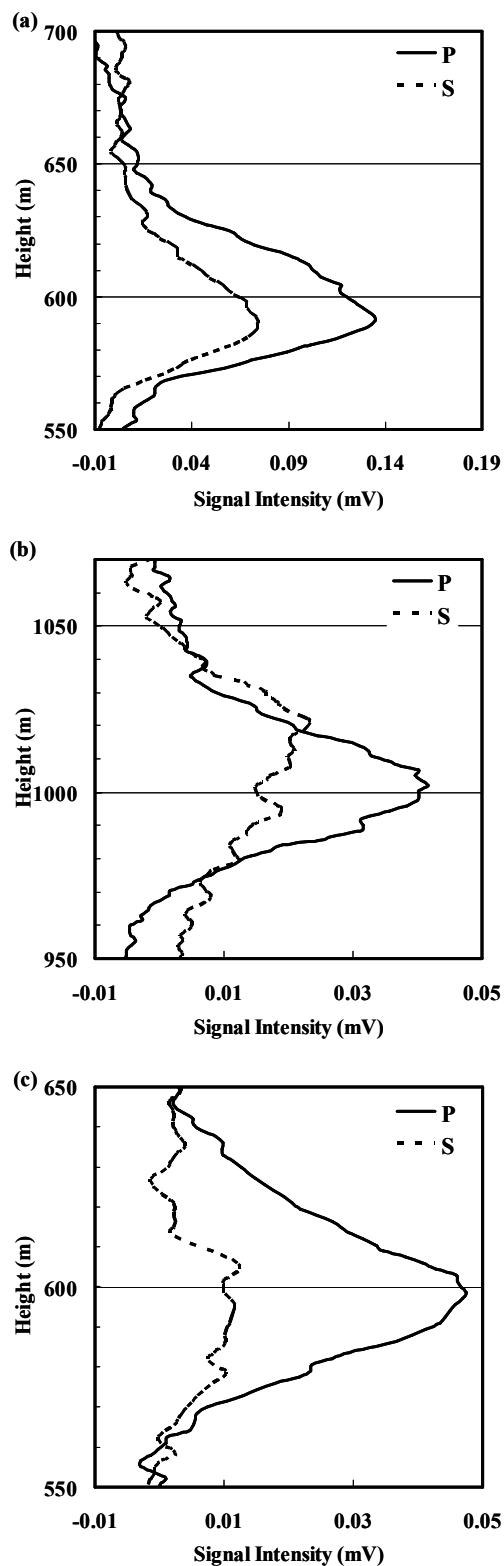
Fig. 2-5. Polarization lidar return from clouds for 450 nm
on 23 March 2005 (a)2:07 (b)2:22 (c)4:41 AM.
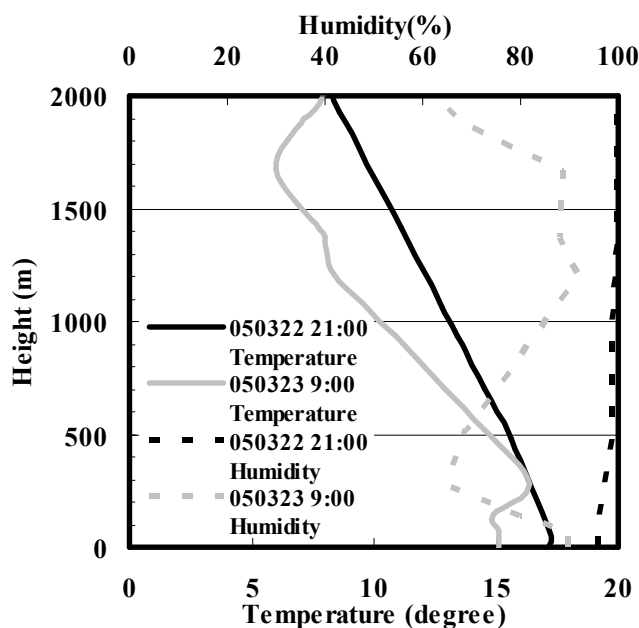
Fig. 2-6. Temperature and humidity as a function of altitude from a radiosonde flight
at 21:00, 22 March 2005 and 9:00, 23 March 2005.

Pal and Carswell observed the tendency to increase the multiple-scattering and depolarization component in case of the lidar source at 347 nm as compared with that at 694 nm. (Pal and Carswell, 1978) Thus, at the 450 nm, the relatively high δ ratios may be partially attributed to the wavelength effect on the forward scattering in these lidar measurements. To provide an explanation of these high depolarization ratios, we need long term observations and the multi-wavelength depolarization lidar measurements in order to evaluate the wavelength dependence as well as the propagation physics of femtosecond laser pulse in atmosphere. However, these results demonstrated the versatility of the white light continuum as a light source of the multi-wavelength depolarization lidar.

2.4. Conclusion

We have observed the depolarization lidar signals for the first time at 450 nm using the coherent white light continuum. Very interesting features of higher depolarization ratios from some clouds layers were also observed. In addition, the present experiment does not fully utilize the potential of the broadband white light continuum. The use of several wavelength-depolarization lidars (Stefanutti et al., 1992) would yield more precise particle size distributions for nonspherical particles such as loess (Asian dust particle) and pollen. Also, lidar measurements using the infrared region (Mejean et al., 2003) of the coherent white light conti-

nuum would yield both the size distributions of relatively large aerosols with radii above 1 μm and the white light differential absorption lidar of gaseous species such as methane or volatile organic compounds (VOCs). The combined use of the depolarization technique and multi-wavelength analysis using the coherent white light continuum will enhance the possibility of deriving information on the particle size distribution.

Chapter 3
Simultaneous Three-wavelength Depolarization Measurements of Clouds and Aerosols Using a Coherent White Light Continuum

First, this chapter introduces an example of simultaneous 3-wavelengths depolarization lidar in tropospheric atmosphere using the coherent white light continuum. Secondly, the time variation of the obtained depolarization ratios was compared with the Angstrom coefficient, which is a good indicator of particle size. Finally, comparisons between experimental data and the simulations based on *T*-matrix method are carried out to estimate how much information can be retrieved about the shape and size of ice crystals in the cloud from three-wavelength depolarization lidar measurements.

3.1. Introduction

Depolarization lidar measurements provide a promising method for distinguishing water and ice clouds and detecting nonspherical particles, because the obtained depolarization ratio is known to depend on the degree of nonsphericity of particles (Sassen, 1991). Theoretical studies showed that nonspherical particle size also exerts an influence on the depolarization ratios

(Mishchenko and Sassen, 1998). Therefore, it can be applied to multi-wavelength depolarization lidar to study the characteristics of aerosols and clouds by using the wavelength dependence of the depolarization ratio (Sugimoto and Lee, 2006; Sassen et al., 2001; Stefanutti et al., 1992). However, the extension of investigations to the multi-wavelength depolarization lidar leads to difficulties in the alignment of the transmission system. Therefore, there is almost no monitoring of clouds and aerosols using simultaneous three- and four-wavelength depolarization lidar (Sassen et al., 2001; Stefanutti et al., 1992). No wavelength dependence of particle shape or size in the depolarization ratio has been shown. An attractive means of overcoming these difficulties could be the use of a coherent white light continuum.

A high-intensity ultrashort pulse focused into a transparent medium generates a white light continuum ranging from the UV to the IR region. These white light continua have spatial and frequency coherence (Nishioka and Ueda, 2003) and deliver intensities over several kilometers under certain conditions (Mechain et al., 2005; Mejean et al., 2005) and are utilized as an ideal light source for lidar (Galvez et al., 2002; Kasparian et al., 2003; Bourayou et al., 2005). Although the current multipass laser amplification system is complex, the system emitting the broader spectrum has the advantages that make it possible to use an arbitrary multi-wavelength probe on the same optical axis. In particular, the IR side of the white light is expected to detect gaseous species such as methane or volatile organic compounds (VOCs) (Mejean et al., 2003). Recently, we observed the 1 wavelength depolarization lidar signals at 450 nm from low-altitude (< 1.0 km) clouds using the coherent white light continuum, and showed that the generated white light continua have the potentiality for multi-wavelength depolarization lidar measurements (Somekawa et al., 2006).

In this chapter, we first show a new white light lidar system designed to permit the simultaneous three-wavelength depolarization measurements, and then present examples of the depolarization measurement from clouds and aerosols using the white light depolarization lidar system. Finally, a new data treatment for a simultaneous three-wavelength depolarization lidar is suggested to infer the size and shape of clouds using a T-matrix simulation.

3.2. Experimental

The femtosecond laser system was described in chapter 2. Briefly, it consists of a Ti:sapphire CPA chain. The final output energy was about 100 mJ per pulse, with a pulse width of 100 fs and a repetition rate of 10 Hz. This femtosecond terawatt laser pulse was focused by a lens with a focal length of 5 m into 9 m long Kr gas cell and converted into the white light con-

tinuum which had a linear polarization similar to the original 800 nm. One of the principal reasons for choosing Kr gas is because it gives a higher intensity at visible region than air. The output beam was transmitted to the zenith collinearly to the axis of the receiver telescope with a 30 cm diameter. The field-of-view (FOV) of the receiver telescope was determined by an iris diaphragm at the focal plane, it was about 1.6 mrad at the minimum aperture. Backscattering light passed along a light guide consisting of a pair of 45° mirrors and was then directed to a three-wavelength depolarization backscattering detection system.

Figure 3-1 shows the three-wavelength depolarization backscattering detection system. The light is spectrally separated by means of dichroic mirrors and bandpass filters. λ/2 plates are placed to line up the polarization axis of the detection system with the polarization vector of the transmitted light. A polarizing beamsplitter cube separates P- and S-polarized light at each wavelength. The detectors are 28 mm diameters photomultiplier tubes used in the analog mode. Each detection unit is aligned by a He-Ne laser. Wavelength properties of the filters, the half-wave plates, and the beamsplitter cubes are given in Table 3-1. In order to detect the more intense signals, the bandpass filter and the half-wave plate at 550 nm have a broadband effective wavelength.
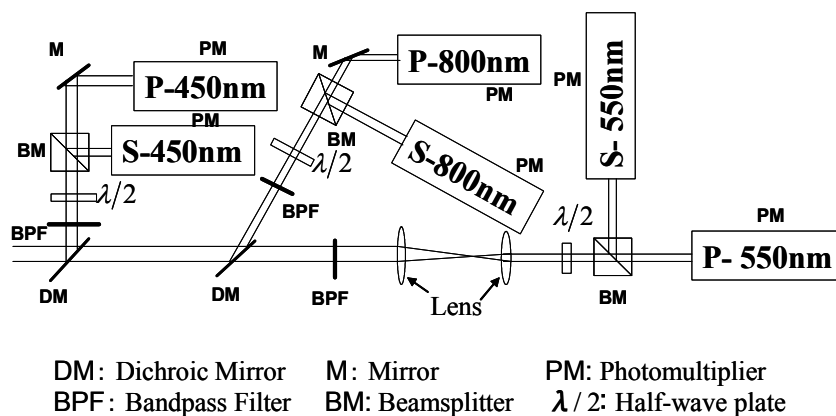
Fig. 3-1. Schematic diagrams of experimental setup of the 3-wavelength depolarization backscattering spectrometer.

Table 3-1. Wavelength properties in beam-separation unit.

	450	550	800
Band-pass filter	457.9 nm (FWHM:10nm)	550 nm (FWHM:40nm)	800 nm (FWHM:10nm)
Half-wave plate	449 nm – 467 nm	460 nm – 655 nm	784 nm – 816 nm
Beamsplitter cube	420 nm – 680 nm	420 nm – 680 nm	620 nm – 1000 nm

3.3. Results and discussion

3.3.1. Observation: A comparison between the depolarization ratios and Angstrom coefficients

The three-wavelength depolarization lidar measurements described in this chapter were obtained during the winter in Feb. 2007 at Suita, Osaka, Japan. The measurements had been performed by integrating over 500 laser shots in order to improve the signal-to-noise ratio. The spacial resolution was determined by the analog-to-digital converter clock frequency of 100 MHz and was 1.5 m. To provide a background signal voltage for each shot, 250 pretrigger points are saved. Also, the background noises came from the lidar system itself, or the sources other than the lidar system such as other light sources were registered when the laser in lidar was blocked and the practical lidar signals were obtained by subtracting these background noises from the actual observed signals. The obtained data were averaged by a running mean of 21 m interval.

The linear depolarization ratio δ is defined as

$$\delta = [S/P]K - \chi, \tag{3-1}$$

where S is polarization orthogonal and P is polarization parallel, the calibration constant K accounts for the difference in both detector channels, and χ is a correction term to account for any mismatch in the transmitter and detector polarization planes. These correction factors were obtained by introducing a strongly attenuated white light into the receiving system using two mirrors before the lidar measurements. We rotated the direction of the $\lambda/2$ plate in front of the polarizing beamsplitter cube and got the correction factors to balance the sensitivity of the polarization channels for three wavelengths.

Figure 3-2 shows an example of 30 min period, simultaneous depolarization profiles at 450, 550, and 800 nm wavelengths. The range squared corrected backscattered signal image of 800P is adopted as a reference profile for the atmospheric information of the observational period. Unreliable values based on too weak signals were deleted from dataset. For reference the radiosonde temperature profiles at a time close to our lidar measurements from nearest weather stations are presented in Fig. 3-3. The station at Shionomisaki (153 km south from lidar site) provided a radiosonde profile at 21:00, 1 Feb. 2007 and 9:00, 2 Feb. 2007.

It can be seen that an image of 800P has different signal intensities in the areas indicated as A. Also, in the area A, the depolarization ratio is nearly zero. This suggested that the particles in area A are water clouds or spherical aerosols. Moreover, this area showed the constant depolarization ratios of ~0 even though the depolarization ratios change in the cloud layer. This demonstrated that the obtained depolarization ratios were not due to fluctuations of the both polarization of the transmitted white light continuum.
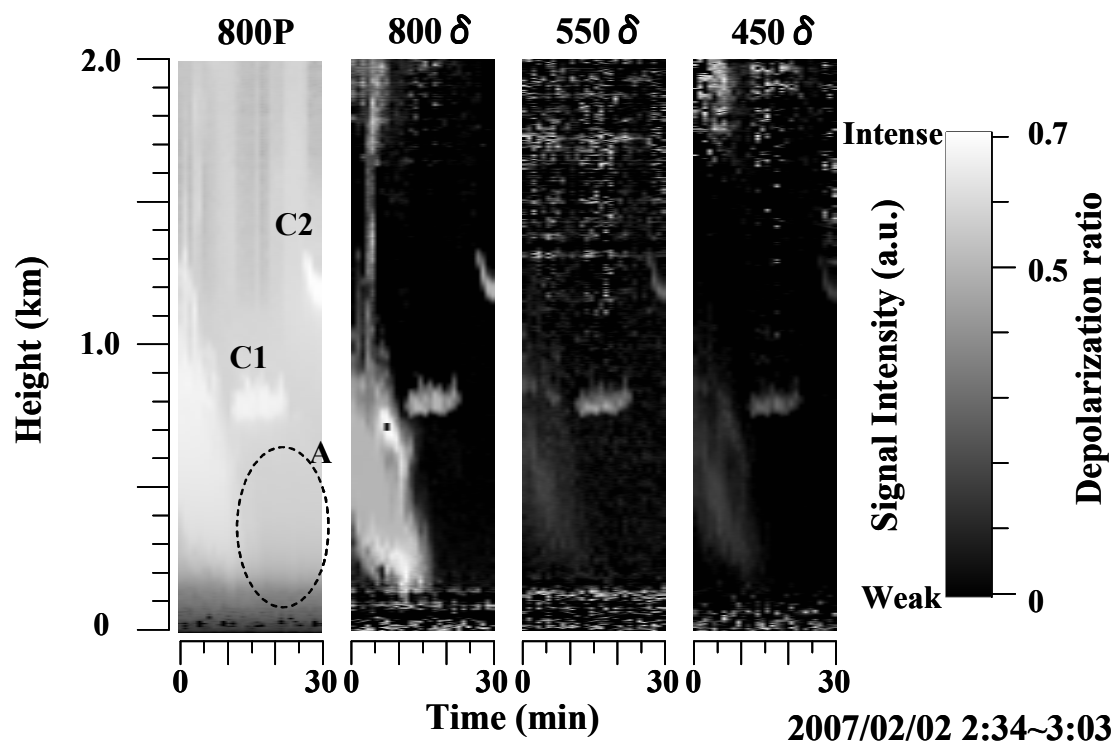
Fig. 3-2. Time height displays for the night of 2 February 2007 from the white light depolarization lidar at Osaka Univ. in Suita, Osaka. 800P is the range squared corrected backscattered signal in relative logarithmic units. 800δ, 550δ, and 450δ give depolarization ratios of the aerosol and cloud layers present.

We also see that the depolarization ratios differ at three wavelengths in clouds indicated as C1 and C2. These clouds didn't show the increase of the depolarization ratios with increasing the penetration depth. Therefore, we considered that the effect of the multiple scattering was not significant in these clouds. Figure 3-4 also exhibits the dependences of the depolarization ratios on the wavelength in the C1 and C2 clouds. The value of the depolarization ratio was decided by using the peak value of depolarization signal in each cloud. The error bars represent the standard deviation for the four profiles in the aerosol layer and are hidden in the plot symbols. The obtained depolarization ratios show convex upward and linear profiles in the C1 and C2

clouds, respectively. This difference allowed us to distinguish the properties of each cloud by measuring the multi-wavelength depolarization ratios of the backscattered signals.

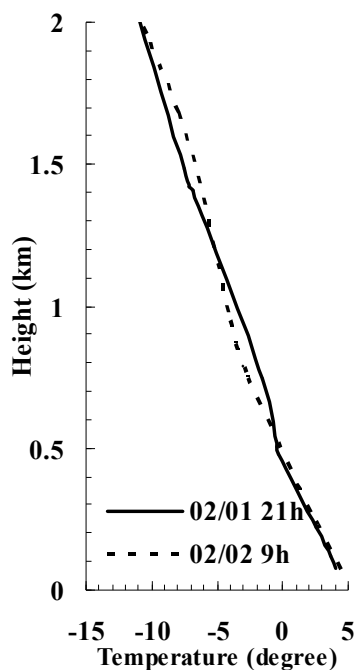Fig. 3-3. Temperature as a function of altitude from a radiosonde flight at 21:00, 1 Feb. 2007 and 9:00, 2 Feb. 2007. The value was derived from the closest weather stations, Shionomisaki, which is about 153 km south of the lidar site.
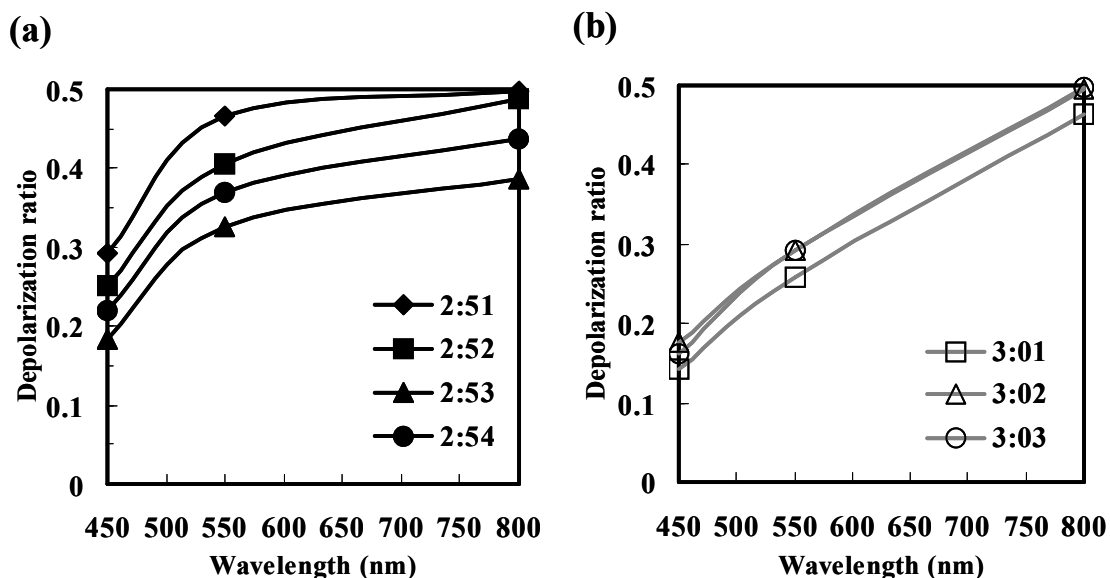
Fig. 3-4. Depolarization ratios from clouds for each wavelength on 2 February 2005: (a) 2:51~2:54 and (b) 3:01~3:03 AM.

We also evaluated the size of the particles in the cloud layers by calculating the backscatter-related Angstrom coefficients and comparing them with the obtained depolarization ratios. In our previous paper (Galvez et al., 2002), we showed the wavelength dependence of the backscatter coefficient β using the white light lidar system. This can be expressed in terms of the Angstrom coefficient, $\mathring{a}$:

$$\beta(\lambda) \propto \lambda^{-\mathring{a}}. \tag{3-2}$$

Thus, the Angstrom coefficient is derived from the backscatter coefficients at 550 and 800 nm:

$$\mathring{a}_{550/800} = -\ln\{\beta(550)/\beta(800)\}/\ln(550/800). \tag{3-3}$$

The Angstrom coefficient is an effective indicator of particle size (Hayashida and Horikawa, 2001). Higher values of $\mathring{a}$ indicate small particles, and smaller values indicate large size particles. However, this approach needs complex inversion algorithms. We derived the backscatter coefficient of the molecular component by using the algorithm of Fernald (1984). The backscatter coefficients for each wavelength were calculated from P + S signal intensity.

Fig. 3-5. The Angstrom coefficients as a function of the depolarization ratios at 550 nm for the C1 and C2 clouds. The data were obtained on 2 February 2005 at 2:51~2:54 and 3:01~3:03 AM.

Figure 3-5 shows an example of the calculated Angstrom coefficient as a function of the depolarization ratios at 550 nm for the C1 and C2 clouds in Fig. 3-4. The Angstrom coefficients in Fig. 3-5 show a positi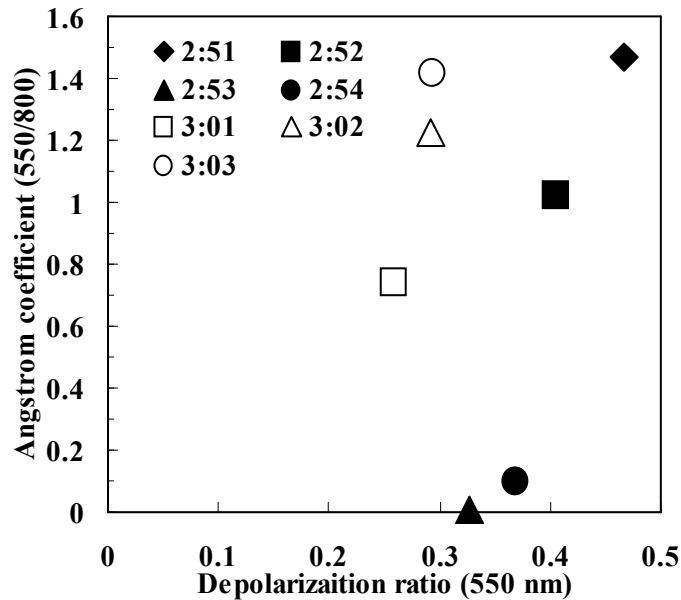ve correlation with the depolarization ratios. This means we can establish a qualitative particle size distribution from the depolarization ratio without any complex inversion process. Moreover, the two different clouds at 2:51 and 2:52 in Fig. 3-4(a) have an almost similar depolarization ratio at 800 nm, but have different depolarization ratios at 450 and 550 nm. From these differences, the multi-wavelength depolarization ratios are more efficient than 1 wavelength depolarization ratio for predicting changes in the particle size. In addition to the above-mentioned interpretation of the observed data, we take the T-matrix method to reproduce the observed depolarization curves and provide the size distribution from the three-wavelength depolarization ratios.

3.3.2. T-matrix computation

We used the T-matrix method and computed depolarization ratios at three wavelengths corresponding to channels on our lidar system for randomly oriented spheroidal particles as estimates for water ice clouds (Mishchenko and Sassen, 1998; Mishchenko and Travis, 1998). In these computations, we have used the shape of particles for the axial ratio $b/a = 1.4$ (a is the horizontal semiaxis and b is the vertical semiaxis), which was assumed to be suitable for the temperature condition at the cloud altitude derived from the radiosonde in Fig. 3-3 (Pruppacher and Klett, 1997). The refractive indices of ice at 450, 550, and 800 nm are $1.3157 + 1.540 \times 10^{-9}i$, $1.3110 + 3.110 \times 10^{-9}i$, and $1.3049 + 1.340 \times 10^{-9}i$, respectively (Warren, 1984). These computations pertain to the power-law size distribution with the effective variance $v_{\text{eff}} = 0.1$. The depolarization ratio δ obtained from the T-matrix computations is defined as $\delta = [F_{11}(180°) - F_{22}(180°)] / [F_{11}(180°) + F_{22}(180°)]$, where F_{11} and F_{22} are the scattering matrix component.

Figure 3-6 shows the evolution of depolarization ratios with increasing the radius. The size of the spheroids is evaluated by the radius of sphere with the equal surface area. For the small particles, it can be seen that the depolarization ratios at 800 nm are close to those at 550 nm, and that these two values are high as compared with those at 450 nm. This tendency is particular true for the experimental results on 2:51 in Fig. 3-4(a). This would seem to indicate that the clouds on 2:51 in Fig. 3-4(a) were relatively small. Furthermore, for the effective radius equal to 1.8 μm, the depolarization ratios decrease in a linear fashion. These depolarization ratio profiles are similar to the depolarization ratio that encounters the clouds observed in Fig. 3-4(b). Similarly, the depolarization profile of 2.4 μm in Fig. 3-6 shows the ranges of the effective radius that reproduces the clouds on 2:52, 2:53, and 2:54 in Fig. 3-4(a). In the large-particle limit,

as shown in the depolarization profile of 3.2 μm in Fig. 3-6, the depolarization ratios are expected to tend to zero. The experimentally determined depolarization ratios are generally found to agree well in their overall trends and behavior. Furthermore, the trend for the size distribution derived from three-wavelength depolarization ratios is comparable to that in the time variation of *å* in Fig. 3-5. This demonstrated that the three-wavelength depolarization ratios provided additional information about size and shape of clouds and aerosols without using complex inversion algorithms.
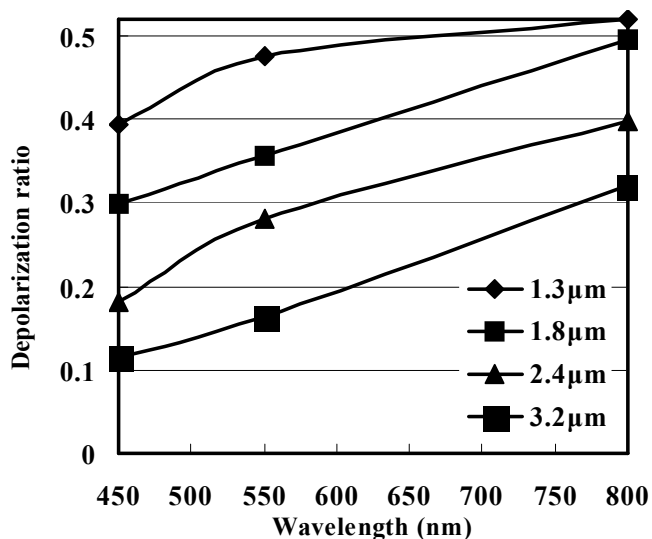
Fig. 3-6. Depolarization ratios computed at 450, 550, and 800 nm
for ice particles of various effective radii.

3.4. Conclusion

The depolarization ratio was simultaneously measured at three wavelengths, 450, 550, and 800 nm, using a coherent white light continuum. The depolarization profiles derived from the *T*-matrix calculation curves fit those of the observed cloud profiles well, which allowed us to evaluate the shape and size of the cloud particles without using complex inversion algorithms. Also, the size evaluation method using depolarization ratios was backed by the Angstrom coefficients obtained by conventional multi-wavelength lidar techniques. Although these methods may not always provide a definitive identification of the shape and size, they can significantly narrow down the plausible range of particle microphysical parameters and can be useful in modeling cloud particle formation and evolution. Further validation of this approach will be undertaken using other favored crystal shapes models and taking into account multiple scattering.

Chapter 4
Observation of Asian Dust Aerosols with Depolarization Lidar Using a Coherent White Light Continuum

Asian dust aerosols originating from the deserts and loess areas of Asian continent are often transported over Japan during the spring season. These Asian dust particles are usually irregular and nonspherical shape, and can be detected by the depolarization lidar. In this chapter, observations of Asian dust aerosols are introduced as a first approach to the environmental problem using the white light depolarization lidar.

4.1. Introduction

The depolarization ratio measured using a lidar is a useful parameter in distinguishing nonspherical particles from spherical particles, and can be used to detect Asian dust particles since most of them have irregular and nonspherical shape. These Asian dust particles are of international interest from the viewpoints of their transport mechanism, radiative effects, and contribution to the geochemical cycle of atmospheric constituents in East Asia and North Pacific regions (Mori et al., 1999; Iwasaka et al., 2003; Sassen, 2002). Therefore, a lidar network for the observation of Asian dust was organized in the spring of 1997 in Japan. The network is expanding internationally and is including Chinese and Korean lidar sites (Murayama et al., 2001).

Asian dust is known as one of the tracers of air pollution, and the cross-border transport of air pollution is a significant environmental issue in Japan (Var et al., 2000; Kim et al., 2003). However, a depolarization lidar has limitations for characterizing nonspherical aerosols because the technique is based on the degree of the nonsphericity of particles. Thus, novel techniques using a lidar for the study of Asian dust particles using a Raman lidar are proposed (Murayama et al., 2004; Tatarov and Sugimoto, 2005). However, if the number of light sources is increased for combined lidar measurement, the transmission system becomes huge and it becomes difficult to align the transmission system. Therefore, we developed a lidar system using a coherent white light continuum (Galvez et al., 2002).

The coherent white light continuum has useful features such as a large spectral extension from ultraviolet to infrared, linear polarization, and an ultrashort pulse duration, enabling multiwavelength measurement and depolarization lidar (Somekawa et al., 2006). Recently, the coherent white light continuum has been applied to laser-induced breakdown spectroscopy (LIBS) (Stelmaszczyk et al., 2004). With these added applications, it is hoped that the white light lidar system can be employed more effectively.

In this chapter, we will describe our white light depolarization lidar system and then report on lidar observations of the dust episode in Osaka. Although the observed depolarization ratio was only at 800 nm, to our knowledge, this is the first white light lidar observation for Asian dust.

4.2. Experimental

Lidar observations were performed mainly in the spring of 2007 (the large Asian dust event happened in May 2007). A white lidar employs a Nd:YAG-laser-pumped Ti:sapphire laser as a light source that generates white light in the wavelength range from 300 nm to more than 950 nm. The final output energy of the Ti:sapphire laser system is typically 100 mJ with a pulse width of 100 fs. The pulse repetition rate is 10 Hz. This femtosecond terawatt laser pulse is focused by a 5-m-focal-length lens into a 9-m-long traveling tube filled with Kr gas at a pressure of 1 atm and converted into a white light continuum with 0.5 TW/100 fs. There are mainly two reasons for selecting Kr gas as a nonlinear material for generating the coherent white light continuum. The first is the high efficiency of conversion to the white light continuum. The second is that a high visible intensity is suitable for lidar measurement (Nishioka and Ueda, 2003). Also, white light generated in Kr gas has a linear polarization similar to that of the original laser (Somekawa et al., 2006).

The receiver telescope has a diameter of 30 cm. Linearly polarized white light is transmitted vertically to the atmosphere, and backscattered light is separated into three wavelengths using dichroic mirrors and interference filters with central wavelengths of 450, 550, and 800 nm having 10, 40, and 10 nm bandwidths, respectively (Somekawa et al., 2008).

The depolarization ratio δ is the ratio of the perpendicular backscattered intensity to the parallel backscattered intensity with respect to the polarization plane of the transmitted white light. δ is computed after adjusting differences in electronic gain and optical misalignment. The accuracy of δ is estimated from the standard deviation for four profiles obtained from a conventional spherical aerosol layer, which is less than 0.004. The details of the lidar system and calibration methods were described in chapters 2 and 3.

4.3. Results and discussion

The white light lidar was operated during the Asian dust events of May 13-14 and 17-18 2007 in Osaka. The presence of Asian dust over our lidar site was predicted by the Chemical Weather Forecast System (CFORS) (Uno et al., 2003), which was actually confirmed by independent measurements using depolarization lidars at the National Institute for Environmental Studies Lidar Network (Murayama et al., 2001).

Figures 4-1(a)-4-1(c) show the height versus time displays of the range squared corrected backscattering and depolarization ratios of aerosol over Osaka on the night of May 2007. We used only 800 nm for the Asian dust depolarization lidar experiment, because it was difficult to obtain large signals at 450 and 550 nm. The vertical resolution was 3 m. The data were smoothed by taking the running mean of the recorded 42-m resolution data to improve the signal-to-noise ratio.

In Fig. 4-1(a), the aerosol layer (about 0.4-1.8 km) for the non-Asian dust event showed a depolarization ratio of about 0, which was taken as the reference between the Asian and non-Asian dust periods. Figure 4-1(b) shows a floating dust layer with a peak at around 1.7 km. Figure 4-1(c) presents a layered structure with 1 to 2 km layer thickness in depolarization ratio. These results are in agreement with the behavior frequently exhibited by Asian dust particles in Japan (Murayama et al., 2001). Additionally, we show in Fig. 4-2 an example of the range squared corrected signal and depolarization ratio for the data shown in Fig. 4-1(b). The range squared corrected signal is shown on the lower abscissa scale and the depolarization ratio on the upper abscissa scale. Note that the aerosols from desert storms are capable of causing stronger

aerosol depolarization at ratios of 0.3-0.7.
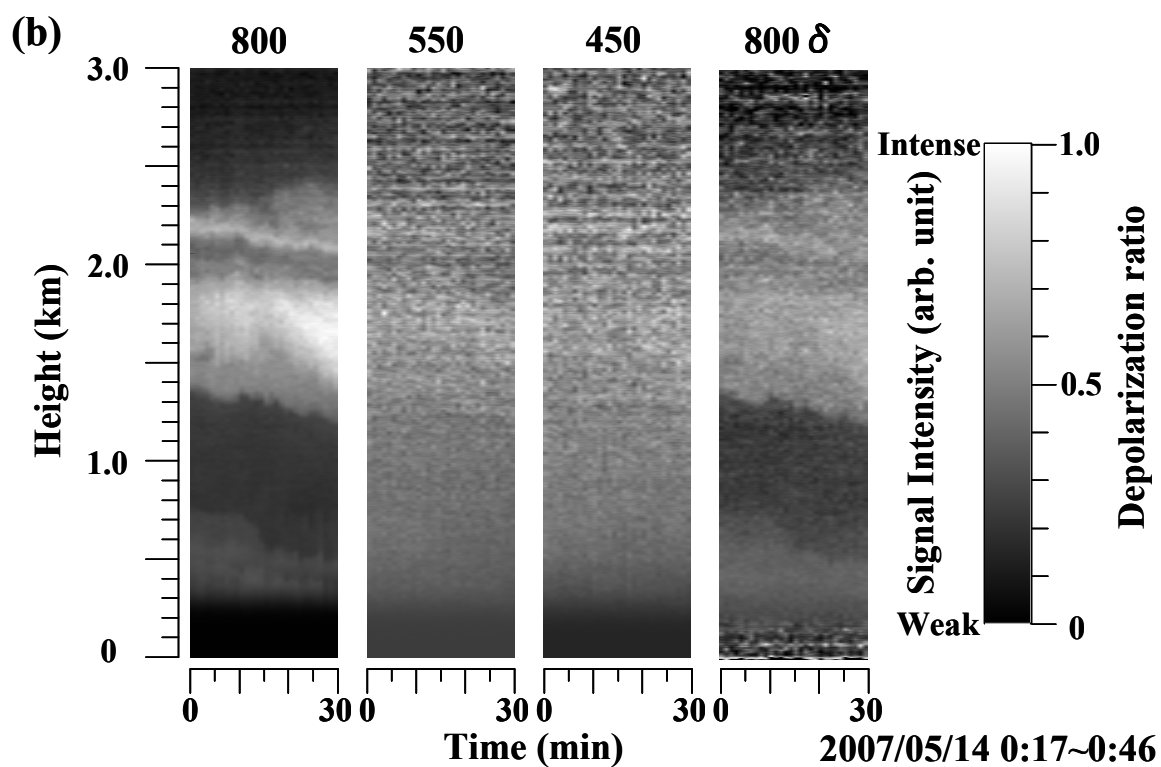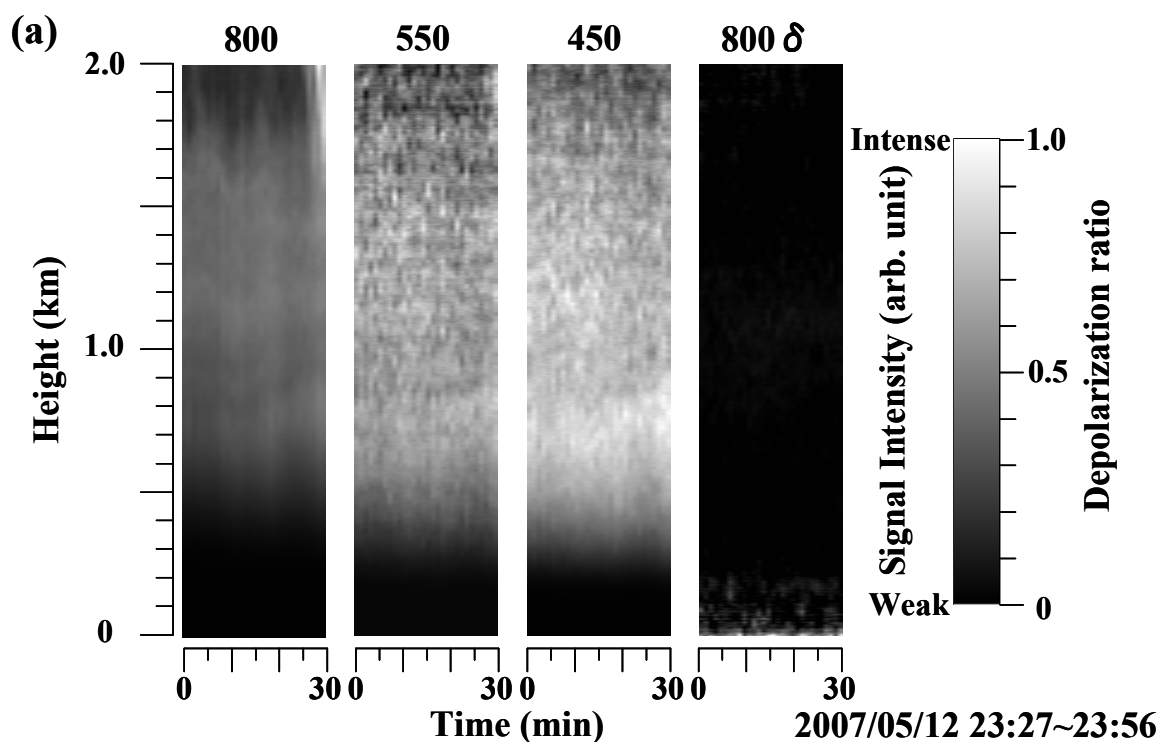
(a)

2007/05/12 23:27~23:56

(b)

2007/05/14 0:17~0:46
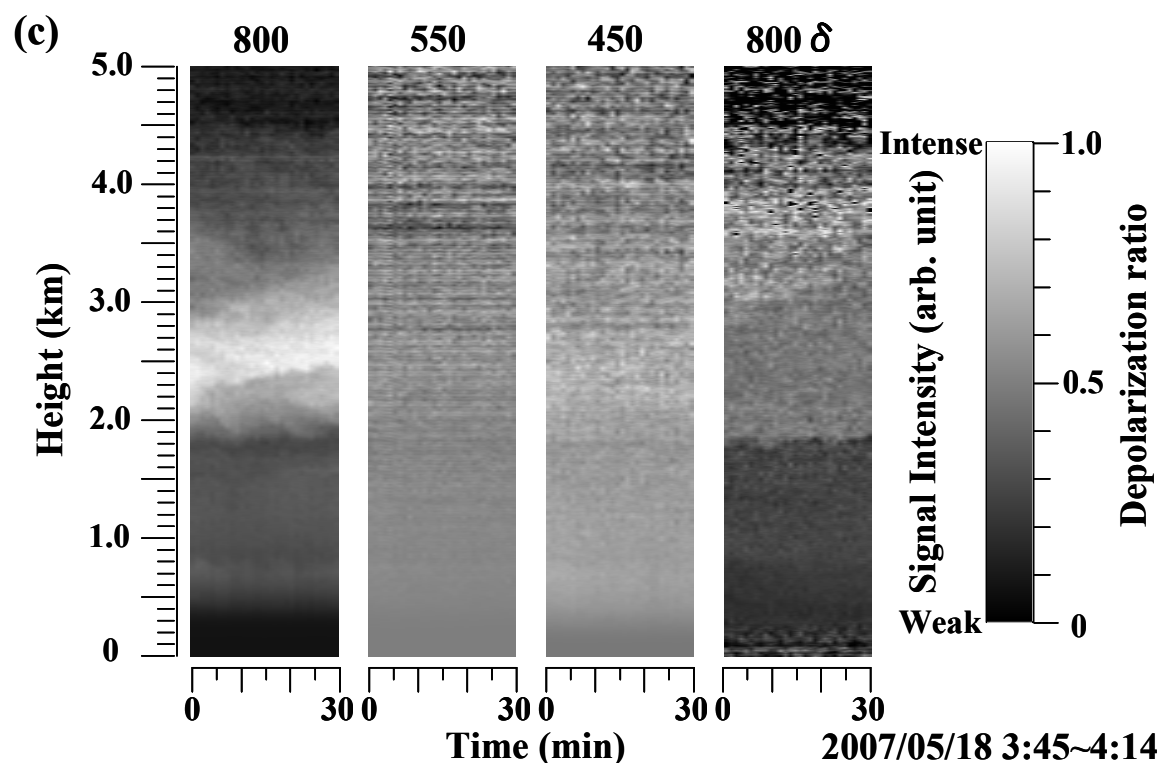
Fig. 4-1. Range squared corrected backscattered power (arbitrary units) and depolarization ratio with white light lidar system on (a) 12 May, (b) 14 May, and (c) 18 May in 2007. The Asian dust covered the Osaka region on May 13-14 and 17-18 2007. We can clearly see the greater depolarization ratio during the Asian dust episodes in Osaka.

A multiwavelength depolarization lidar technique has potential for inferring the shape and size of aerosols without the assumptions required for conventional multiwavelength Mie lidar analysis (Somekawa et al., 2008). Although Asian dust particles were detected at 800 nm in this study as suggested from the high depolarization ratios, the depolarization ratios at 450 and 550 nm could not be obtained because of the weak S-polarization signals. The main reason for this is that the white light intensity at 450 or 550 nm is about two orders of magnitude weaker than that at 800 nm. In addition to the weak intensity in both bands, the climate conditions also affected our observations. The aerosol layer on these occasions were not visually observed, namely the Asian dust particles were rather tenuous.

The depolarization ratios in lidar experiments generally show a wavelength dependence, and the ratio for 800 nm is expected to be larger than that for 450 or 550 nm (Sugimoto and Lee, 2006). The enhancement in the depolarization ratios at longer wavelengths was explained by our T-matrix computation (Somekawa et al., 2008). Such differences in wavelength are important,

since, for example, they would result in the sensitive detection of Asian dust particles. However, in the white light depolarization lidar, it remains possible that the obtained depolarization ratios are affected by fluorescence because of the broadband characteristics including the ultraviolet region. In fact, Mejean et al. (2004) demonstrated the detection of remote biological aerosols by the two-photon laser induced fluorescence using femtosecond terawatt laser pulses. Generally, fluorescence is unpolarized and we should need correction owing to the effect of fluorescence, e.g., a comparison of the depolarization ratios at 800 nm between the coherent white light continuum and the fundamental 800 nm laser as a lidar light source. Furthermore, the contributions of multiple scattering to the backscattered depolarization ratios are important and have been investigated for scatters with high optical depth. This effect induces depolarization signals (Pal and Carswell, 1973). The multiple field-of-view (FOV) lidar experiment that we are performing now will clarify the effect of multiple scattering.
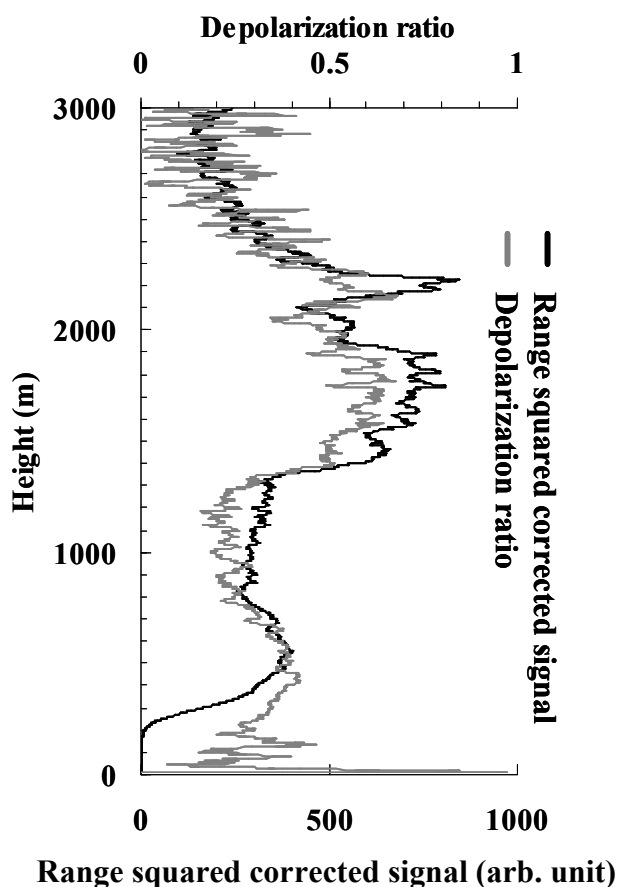
Fig. 4-2. Range squared corrected signal and depolarization ratio from Asian dust layers for 800 nm on 14 May 2007 at 0:17 AM.

4.4. Conclusion

We observed an aerosol layer with strong depolarization corresponding to the Asian dust event. Thus, for the first time, Asian dust particles were sampled using the white light lidar with polarization diversity that enables the assessment of the degree of particle nonsphericity. The obtained depolarization ratios were higher at 0.3-0.7 than their usual value of ~0. The discussions are based on the measurements made in May 2007 at Osaka and do not cover a sufficiently long time for us to definitely conclude the characteristics of Asian dust particles. Long-term monitoring of Asian dust is necessary in future research. However, the advanced white light lidar is expected to be an essential tool for the characterization of complex aerosols.

Chapter 5

Dependence of the Multiple Scattering Depolarization on the Wavelength Using the White Light Lidar System

Subsequent steps in our white light depolarization lidar are described in this chapter. As described in section 2.1, the depolarization ratios are affected by the multiple scattering. Conversely, the depolarization ratios of multiple scattering may include additional information that causes the multiple scattering. Thus, the multiple field-of-view (FOV) lidar measurement and evaluation based on a simple two-FOV method are discussed.

5.1. Introduction

The information content of lidar signals is enhanced by adding depolarization measurements. This principle of operation is well known and based on the simple fact that single backscattered light from spherical particles retains the polarization of the incident light, but irregularly shaped particles cause significant depolarization. If the receiver FOV is sufficiently wide to collect backscattered light that is including the multiple scattering at not exactly 180° but other scattering angle, the obtained signals become depolarized even for the spherical particles

(Sassen and Zhao, 1995; Bissonnette et al., 2001). However, this opens up the possibility to retrieve the additional information about cloud droplet size or the particle size density distribution by determining the polarization characteristics of multiple scattering (Tatarov et al., 2000).

In this chapter, we report the wavelength dependence of multiply scattered lidar returns. The lidar observations are performed by using a multiple-FOV three-wavelength depolarization lidar derived from our white light depolarization lidar system (Somekawa et al., 2008).

5.2. Experimental

The observations were carried out using a three-wavelength depolarization lidar with a variable receiving FOV. The design of the system was based on an already operating white light depolarization lidar (Somekawa et al., 2008). A chirped-pulse amplification femtosecond (typically 100-fs, 100mJ, 800 nm) pulses at a 10-Hz repetition rate are focused with a long-focal length lens ($f = 5$ m) on Kr gas and converted into the coherent white light continuum which has a broad spectrum from 300 nm to more than 950 nm and a linear polarization similar to the incident 800 nm laser. The receiver consists of the 30 cm primary mirror Newtonian telescope and the colleted light is recorded by using 3 filter sets: 450, 550, and 800 nm. In addition, this system has an iris diaphragm at the focal plane of the receiving telescope and the FOV of lidar measurements is variable. The experimental data are acquired consecutively by changing an iris placed at the focal of the telescope corresponding to FOV of 1.6 and 4.0 mrad. The interval between the two-FOV measurements is 1 minute.

5.3. Results and discussion

Figure 5-1 shows the depolarization ratios at 450, 550, and 800 nm observed in Osaka, Japan, in February 2007. The depolarization ratio, δ, is defined as the ratio of the perpendicular signal (S-polarization) to the parallel signal (P-polarization). 800P presents the range squared corrected signal profile for a channel with P-polarization at 800 nm as a reference profile for the atmospheric information of the observational day. On 2 February 2007, thin clouds were identified during the multiple FOV measurement. From 800P profile we can show that these clouds, with thickness of about 300 m, were identified at about 1.0 km altitude. An aerosol layer was identified below the clouds. In the aerosol layer, the depolarization ratios are almost zero, indicating spherical particles. In comparison, the depolarization ratios are considerable stronger in the ice clouds.

Figure 5-2 indicates the depolarization ratios and the Angstrom coefficients, which is a good indicator of particle size, derived from the observations. As shown in Fig. 5-2(a), the depolarization ratios with 4.0-mrad FOV were larger than that with 1.6-mrad FOV. These results seemed to be in good agreement with the previous paper which the multiple scattering induced the depolarized signals (Pal and Carswell, 1973). However, since the Angstrom coefficients in Fig. 5-2(b) showed the same tendency as the depolarization ratios, such differences are attributable mainly to temporal variations in cloud particle size. Thus, in order to determine the change in the depolarization ratio due to multiple scattering, it is necessary to acquire lidar return signals with the same size distribution.
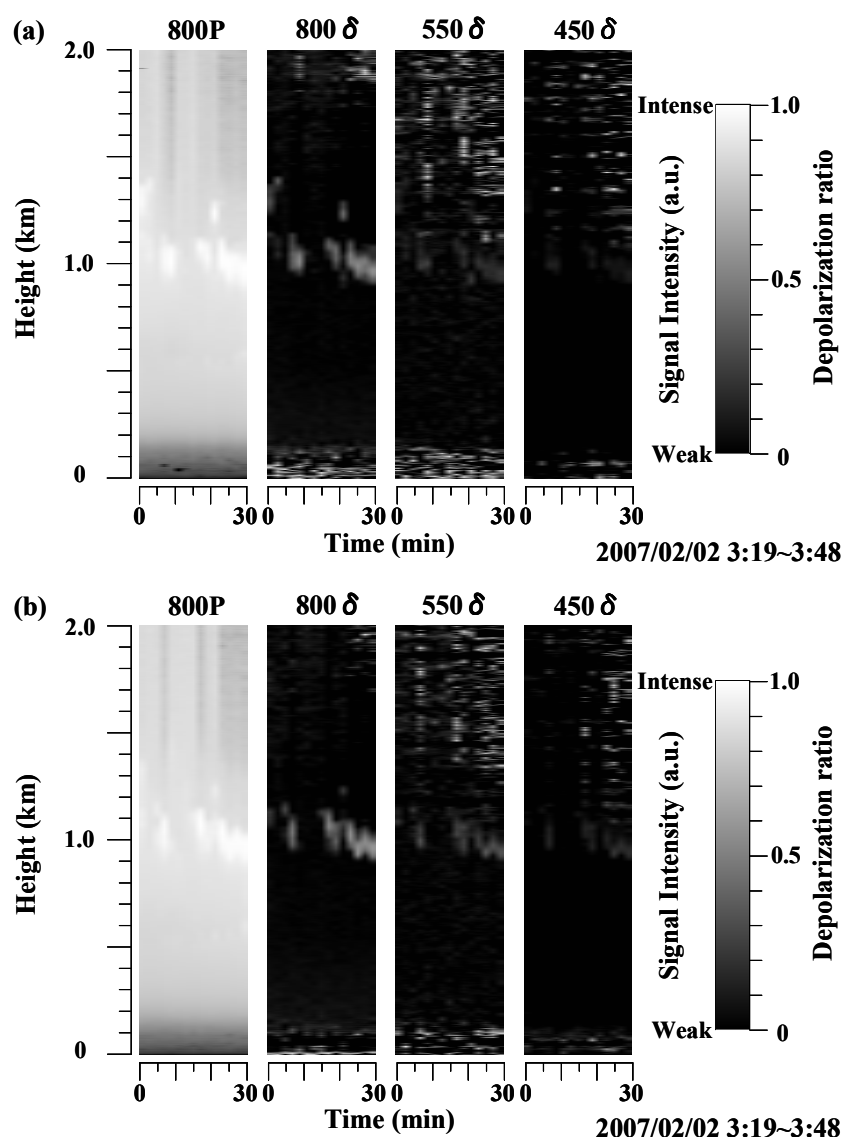
Fig. 5-1. Time-to-height indication of the range squared corrected backscattering intensity and the depolarization ratio on February 2, 2007, obtained at Osaka University. Receiver field of view: (a) 1.6 mrad, (b) 4.0 mrad. Time interval between the two measurements is 1 minute.
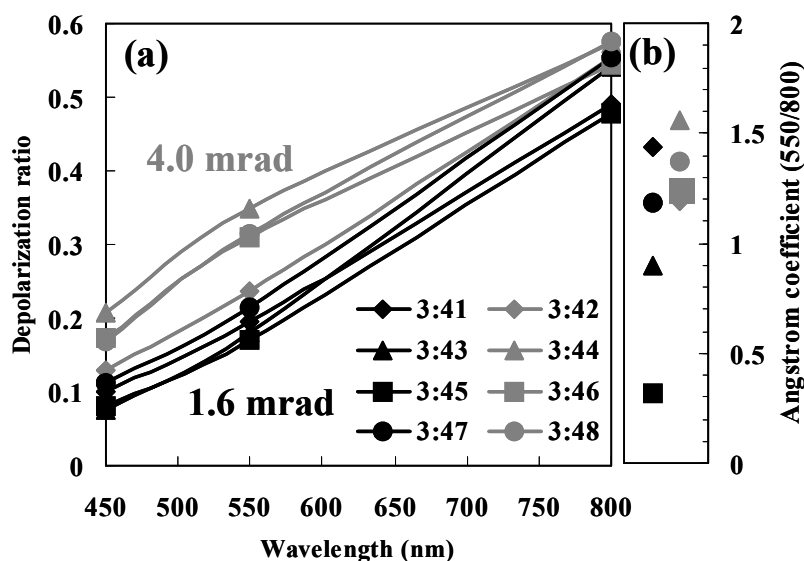
Fig. 5-2. (a) Measured depolarization ratios as functions of wavelength and (b) corresponding Angstrom coefficient. Black and gray symbols denote 1.6 and 4.0 mrad FOV measurements, respectively.

In order to calculate the depolarization ratio due to multiple scattering, we concentrate our quantitative analysis on two particular clouds of the observations in Fig. 5-1. These sets of clouds shown in (a) and (b) of Fig. 5-3 have almost the same Angstrom coefficient, we can assume to be the same size distribution. Since the depolarization ratio with a large FOV, $\delta_{4.0}$, involves that with a small FOV, $\delta_{1.6}$, we obtained depolarization ratios due to multiple scattering by subtracting $\delta_{1.6}$ from $\delta_{4.0}$.
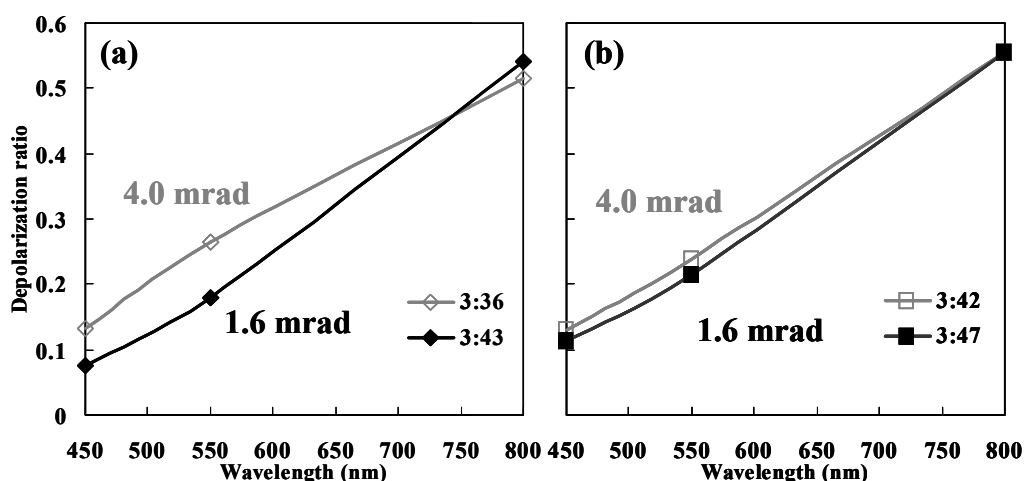
Fig. 5-3. The wavelength dependence of the measured depolarization ratios on the almost same size distribution with receiver FOVs of 1.6 mrad and 4.0 mrad.

We studied the effect of multiple scattering on the depolarization ratios at 450, 550, and 800 nm with a simple two-FOV model. We introduce the multiple-scattering fraction, Y, such that

$$Y = I_{1.6}/ I_{4.0},$$ (5-1)

where $I_{1.6}$ and $I_{4.0}$ are the range squared corrected total-scattering (single + multiple) lidar back-scatter signal with 1.6-mrad and 4.0-mrad FOV, respectively. Using Y, the parallel and perpen-dicular components of the backscattered light are written as follow:

$$I_P = \frac{IY}{1 + \delta_{1.6}} + \frac{I(1 - Y)}{1 + \delta_m},$$ (5-2)

$$I_S = \frac{\delta_{1.6} IY}{1 + \delta_{1.6}} + \frac{\delta_m I(1 - Y)}{1 + \delta_m}.$$ (5-3)

Here, δ_m is the depolarization ratio due to multiple scattering for the FOV from 1.6- to 4.0-mrad. Consequently the depolarization ratio with a 4.0-mrad FOV is determined by the following equation:

$$\delta_{4.0} = \frac{\delta_m(1 + \delta_{1.6}) + Y(\delta_{1.6} - \delta_m)}{(1 + \delta_{1.6}) - Y(\delta_{1.6} - \delta_m)}.$$ (5-4)

Conversely, the depolarization ratio δ_m can be determined from the observed polarization ratio as follow:

$$\delta_m = \frac{\delta_{4.0}(1 + \delta_{1.6} - Y\delta_{1.6}) - Y\delta_{1.6}}{(1 + \delta_{1.6}) - Y(1 + \delta_{4.0})}.$$ (5-5)

This equation is an extension of that used for estimating the depolarization ratio in a mixture of spherical and nonspherical aerosols in previous papers (Sugimoto and Lee, 2006). We adopted the peak δ values observed with lidar in atmospheric clouds. The calculated values of δ_m derived from our model are listed in Table 5-1.

Table 5-1. Two FOV model parameter.

		(a)		(b)	
		3:36	*3:43	3:42	*3:47
Angstrom coefficient (550/800)		0.877	0.901	1.19	1.19
Y	800	0.905		0.908	
	550	0.693		0.906	
	450	0.739		0.904	
δ_m	800	0.306		0.550	
	550	0.507		0.290	
	450	0.327		0.179	
$\delta_m/\delta_{1.6}$	800	0.564		0.991	
	550	2.81		1.35	
	450	4.28		1.58	

* Receiver FOV of 1.6 mrad

Figure 5-4 shows the wavelength dependence of the normalized multiple scattering depolarization ratios. This parameter $\delta_m/\delta_{1.6}$ is utilized in conjunction with $\delta_{1.6}$ to characterize more fully the wavelength dependence of δ_m. The values of $\delta_m/\delta_{1.6}$ show a tendency toward increasing values as the wavelength decreased. The differences in $\delta_m/\delta_{1.6}$ at small wavelength are likely to be due to the wavelength dependence in the multiple scattering as a result of the wavelength effect on the forward scattering (Pal and Carswell, 1978).

The multiple scattering seems to be associated with the change in optical depth that results from a change in particle number density. The relationship of the particle size and optical depth is reported to be a negative correlation such that the particle size increases as the optical depth decreases (Nakajima et al., 1991). Therefore, as already seen from the Angstrom coefficients, the optical depth in Fig. 5-3(a) may be smaller than that in Fig. 5-3(b) considering that the Angstrom coefficients are larger in a smaller particle size. In fact, the optical depth at 1.6-mrad FOV in Fig. 5-3(a) and Fig. 5-3(b) was determined to be 0.733 and 0.783 at 800 nm, respectively, as the integral of extinction coefficient from cloud bottom to cloud top. Thus, in the low optical depth cloud as shown by ♦ symbols in Fig. 5-4, the $\delta_m/\delta_{1.6}$ values show a large increasing trend as the effect of the above-mentioned forward scattering become more dominant. On the other hand, the depolarization ratio δ_m approaches the value for backscattering at 180 for greater penetration depth (Reichardt and Reichardt, 2003). In the cloud of large optical depth the penetration depth may be considered to be greater than in clouds with small optical depth. As a

result, the values of $\delta_m/\delta_{1.6}$ have a small slope and approach 1.

Furthermore, it is assumed, as in Eck et al. (1999), the slope of the optical depth versus the wavelength on the logarithmic scale provides an excellent fit to a second-order polynomial curve. In agreement with our expectations concerning the wavelength dependence of depolarization ratios, $\delta_m/\delta_{1.6}$ values can be seen to increase quadratically with decreasing wavelength. Thus, shown in Fig. 5-4, the variations in the approximate multiple-single scattering ratio, $\delta_m/\delta_{1.6}$, may contain additional information regarding the cloud number density.
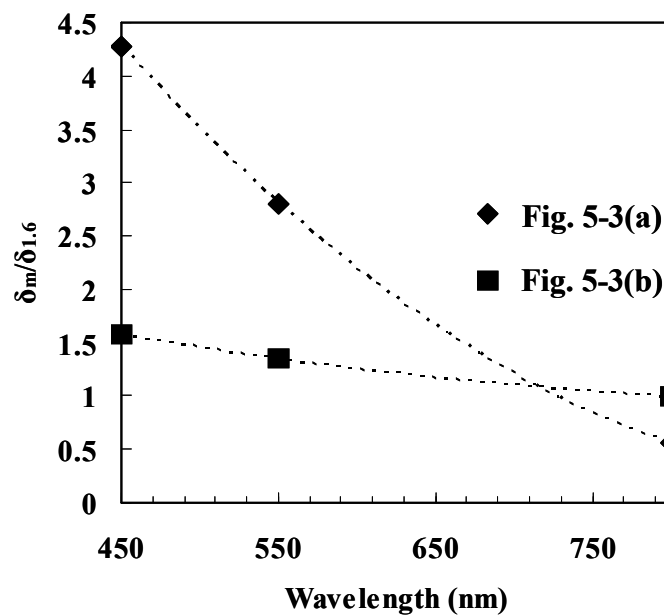
Fig. 5-4. The wavelength dependence of ratios of multiple-scattering (δ_m) to the narrow FOV ($\delta_{1.6}$) depolarization ratio at cloud.

5.4. Conclusion

As a preliminary test of the multiple scattering depolarization ratio routines outlined in this chapter, the multiple-FOV data from the white light depolarization lidar experiments were analyzed. This approach allows us to evaluate the multiple scattering contributions to the lidar depolarization ratio and to obtain the number density of clouds. Such future enhancements to the white light lidar technique should allow improved simultaneous measurements of the particle size, shape, and the number density.

Chapter 6

A New Concept to Characterize Nonspherical Particles from Multi-wavelength Depolarization Ratios Based on *T*-matrix Computation

This chapter presents a case study of nonspherical particles in an ice cloud through lidar measurements coupled with *T*-matrix simulations. Section 6.2 presents a review of the parameters of the *T*-matrix lidar simulations. Results and discussion are presented in section 6.3.

6.1. Introduction

A method for measuring aerosol size is required to study the effect of aerosols on the radiative transfer processes of the atmosphere concerning climate change. Several lidar methods were reported for obtaining particle size information of aerosols and clouds; these are lidars using multi-wavelength Mie scattering lidar, multiple-field-of-view lidar, and Raman scattering lidar (Roy et al., 1999; Whiteman et al., 1999). However, these approaches need complex inversion algorithms to derive the desired quantities. Also, the measurement of the size distribution

of dust particles can be difficult due to the irregular and nonspherical shapes.

In this chapter, we describe another simple method using *T*-matrix computation. This method utilizes the dependence of depolarization ratio on wavelength. The depolarization ratio is defined as the ratio of orthogonal to parallel polarized backscattered signals. Depolarization lidar is a powerful remote sensing method for distinguishing between the spherical particles and nonspherical particles. We recently described a depolarization lidar using a coherent white light continuum (Somekawa et al., 2006), which can develop a new lidar system to detect the multi-wavelength depolarization ratios. The white light lidar has an advantage of measuring a number of atmospheric species without limiting the observation wavelength due to the laser emission wavelength.The new lidar system consisted of three depolarization channels at 450, 550, and 800 nm. Therefore we calculated the wavelength dependence of the ratio of the polarization component for an ice cloud at these three wavelengths. Furthermore, we provide an interpretation of the previous observation results using a simple two-component model.

6.2. *T*-matrix computations

We use the *T*-matrix method and compute depolarization ratios for polydispersions of randomly oriented spheroidal particles as estimates for ice clouds. The FORTRAN *T*-matrix codes are publicly available on the World Wide Web at http://www.giss.nasa.gov/~crmim in the "extended-precision *T*-matrix code for randomly oriented nonspherical particles" versions. This version can be applied to significantly larger particles such as clouds particles (e.g., Mishchenko and Sassen, 1998; Mishchenko and Travis, 1998 and references therein).

The refractive indices of ice at 450, 550, and 800 nm are $1.3157 + 1.540 \times 10^{-9}i$, $1.3110 + 3.110 \times 10^{-9}i$, and $1.3049 + 1.340 \times 10^{-7}i$, respectively (Warren, 1984). The shape and size of particles can be specified by the axial ratio b/a (a is the horizontal semi-axis and b is the vertical semi-axis) and the radius of a sphere having the same surface area. The results were computed with an effective radius step size of $\Delta r_{eff} = 0.1$ and the effective variance of $v_{eff} = 0.1$ at 450, 550, and 800 nm lidar wavelengths.

The depolarization ratio δ can be described by the scattering matrix component *F*

$$\delta = \frac{F_{11}(180°) - F_{22}(180°)}{F_{11}(180°) + F_{22}(180°)}$$ (Mishchenko and Sassen, 1998). (6-1)

For spherical particles $F_{11}(180°) = F_{22}(180°)$, thus the single scattered signals are not depolarized. Indeed, for slightly nonspherical particles with $b/a = 0.999$ depolarization ratios are nearly zero.

6.3. Results and discussion

Figure 6-1 shows the depolarization ratios of *T*-matrix computations for randomly oriented spheroidal particles as estimates for ice clouds. We assumed two ice crystal habits with (a) -4 to -9, (b) -9 to -23 ℃ (Pruppacher and Klett, 1997). The inserts in Figures show the respective particle shapes. The convergence of the *T*-matrix code poses an upper limit to the applicable size range.

In this simulation, a modified power law distribution is assumed to describe the range of particle sizes within the clouds. In the 800 nm curves of Fig. 6-1(a), the dashed and dotted line show the depolarization ratios derived from the log normal and gamma distribution with the same $v_{eff} = 0.1$, respectively. This showed that different distribution shapes do not cause significant difference in the depolarization ratio. Furthermore, the modified power law size distribution has the important practical advantage of being able to reduce computation time. Hence, the particle sizes discussed in this chapter have been determined by the effective radius r_{eff} of the modified power law distribution.

It can be seen in both depolarization curves in Figs. 6-1(a) and 6-1(b) that the depolarization ratios are rapidly increased with increasing r_{eff} from 0 to about 1 μm, have maximal values for the small particle, and decrease gradually as the effective particle size increases. As the wavelength ranges from 450 nm to 800 nm, the peak is shifted to larger effective radius. The most notable differences due to the shape are after maximal depolarization ratio.

In Fig. 6-1(a), the depolarization ratios decrease with particle size monotonically. As the result, the depolarization ratio for particles with a larger radius shows a larger wavelength dependence. This is in good agreement with the actual observations with the depolarization ratio for 1064 nm always being larger than that for 532 nm (Sugimoto and Lee, 2006).

Figure 6-1(b) shows that the depolarization ratios have smaller maximal values than those for ice prolate spheroid and approach a value of about 0.3. This appears to explain the frequent occurrence of depolarization ratios ranging from 0.35 to 0.7 for the conventional lidar observations (Sassen et al., 1990).

The results presented in Fig. 6-2(a) demonstrate the potentialities to characterize the particle size from three-wavelength depolarization ratios. The depolarization ratios are shown as a function of the wavelength for various effective radiuses. Figures 6-2(a) and 6-2(b) correspond to Figs. 6-1(a) and 6-1(b), respectively. For small particles, it can be seen that the depolarization ratios at 800 nm are close to those at 550 nm and these two values are high as compared with those at 450 nm. This tendency shows the profile of a convex upward depolarization curve. When the radius increases, the depolarization ratios decrease in a linear fashion. In the large-particle limit, the depolarization ratios are expected to tend to zero. These calculated depolarization curves are similar to the change of those against wavelength that was observed by our white light depolarization lidar system (Somekawa et al., 2008).

The results show that effective radius can be determined by plotting the observed depolarization ratios against wavelength and comparing them with the theory. Thus the multi-wavelength depolarization ratios are very useful for characterizing nonspherical particles, although the computations are limited in ice clouds. Moreover, as seen in Fig. 6-2(a), although the depolarization ratios in 1.1 and 1.5 μm have an almost similar value at 800 nm, they have significant difference at 450 and 550 nm. Thus, multi-wavelength depolarization measurements are more efficient than 1-wavelength depolarization measurements for inferring changes in the particle size.

The shape of aerosols will affect an error in estimating the effective radius. For ice cloud with the larger effective radius shown in Fig. 6-2(b), the retrieved size distributions are insensitive with respect to variations of the effective radius. However, this method can significantly narrow down the plausible range of particle microphysical parameters.
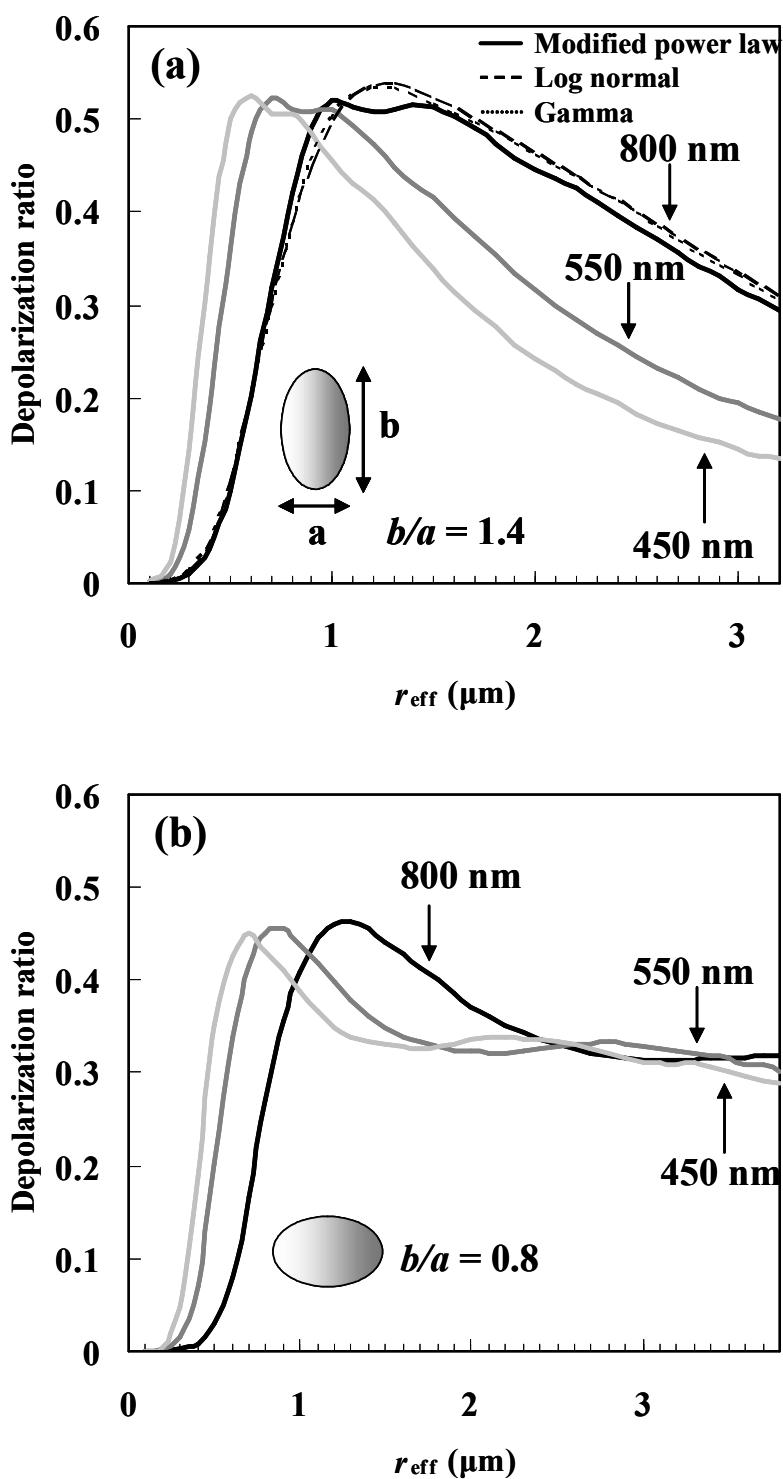
Fig. 6-1. Depolarization ratio versus effective radius for two ice crystal habits with (a) -4 to -9, (b) -9 to -23℃. In 800 nm curves in (a), the depolarization ratios for modified power law, log normal, and gamma size distribution that have the same effective variance $v_{eff} = 0.1$ were presented for comparison.
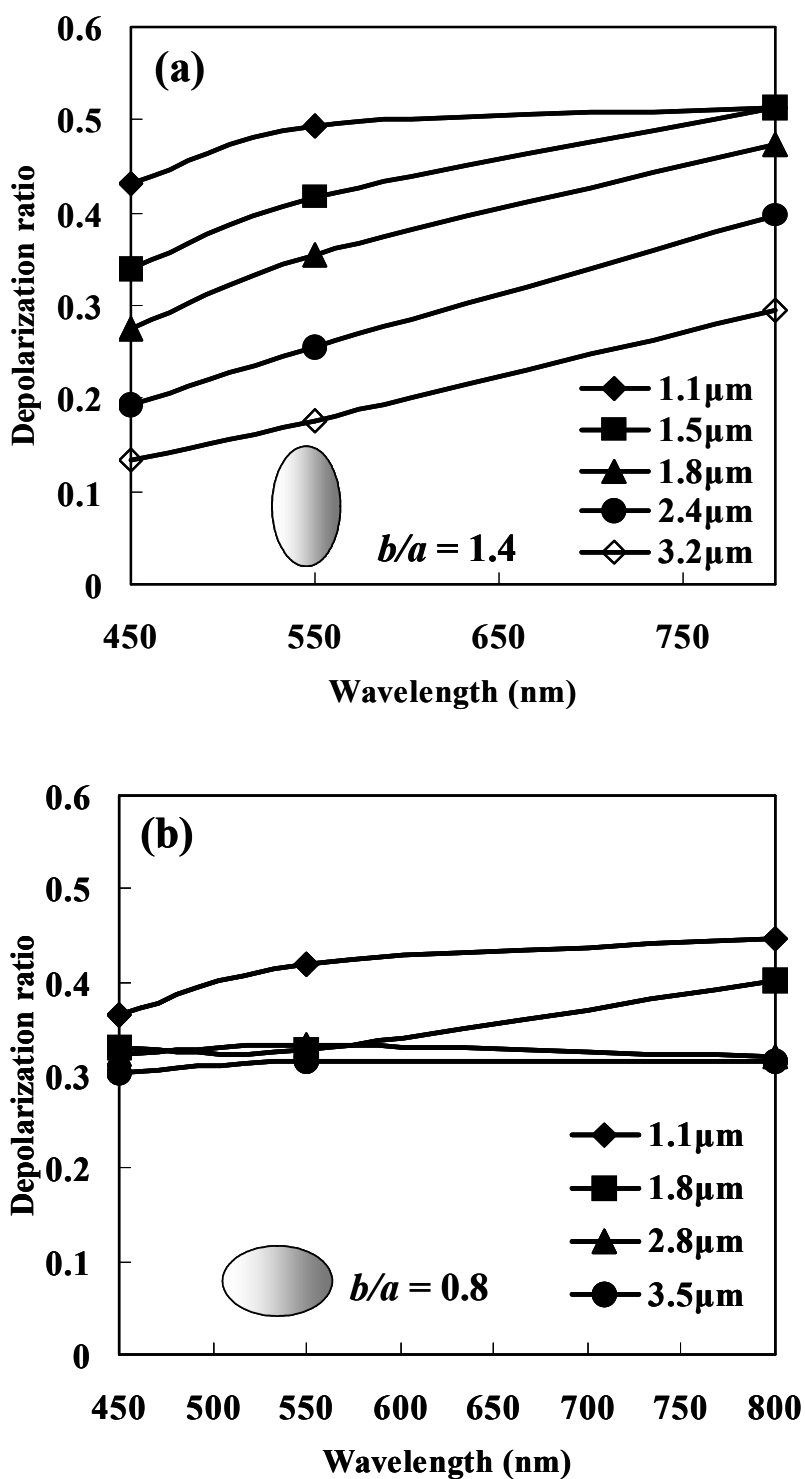
Fig. 6-2. Depolarization ratios versus wavelength for (a) prolate and (b) oblate ice particles of various effective radiuses.

Sassen et al. (2001) performed depolarization lidar observations at 532, 694, and 1064 nm. However, there was only one case that was used for intercomparison. The depolarization ratios at about 9-km cirrus layer range from 0.22 at 532 nm and 0.22 at 694 nm, to 0.25 at 1064 nm, indicating the same wavelength dependence of our calculations. There are two possibilities to explain δ values less than our calculations. One explanation is that large particles whose radii are larger than the calculated limit predominantly exist in the air, and other explanation is that spherical and nonspherical particles coexist in the air.

The depolarization ratio for atmospheric aerosols should be dependent on the particle size. Also, it may depend on the internal mixing state because the spherical particle causes no depolarization. We present results for a more realistic case in which the mixing of ice clouds and water clouds is taken into account with a simple two-component model (Sugimoto and Lee, 2006). We introduce the mixing ratio of ice *X*, which is defined as the ratio of ice cloud to cloud water of all phase. The depolarization ratio δ_X for the mixture is given by

$$\delta_X = \frac{\delta X}{X + (1 - X)(1 + \delta)}.$$

(6-2)

Here δ is the depolarization ratio of *T*-matrix computation for ice particles at each wavelength. The depolarization ratios at 532, 694, and 1064 nm were calculated by following the same procedure as for our lidar wavelengths. We have used graphical interpolation to get the refractive indices of ice from the particular wavelengths shown in Warren (1984). The obtained refractive indices at 0.532, 0.694, and 1.064 μm are $1.3117 + 2.7 \times 10^{-9}i$, $1.3070 + 2.6 \times 10^{-8}i$, and $1.3004 + 1.9 \times 10^{-6}i$, respectively. The computed depolarization ratio for nonspherical particles with the axial ratio *b/a* = 0.8 is presented in Fig. 6-3(a).

We apply the depolarization ratios shown as r_{eff} = 2.3 μm in Fig. 6-3(a) to Eq. (6-2). Figure 6-3(b) illustrates the dependence of mixing ratios on the depolarization ratio δ_X that reproduces the observed values at 532, 694, and 1064 nm. Measured values of depolarization ratios at three-wavelength by Sassen are presented by ◊ symbols in Fig. 6-3(b).

The observed depolarization behavior is indeed well reproduced by the effect of the mixing of spherical and nonspherical particles. The mixing ratio of *X* = 0.7 as obtained by the simple two-component model corresponds well to the depolarization ratios at three-wavelength by Sassen. Moreover, the depolarization ratios decrease as the mixing ratio decrease. As a result, the existence of water droplet causes the depolarization ratio to be underestimated.
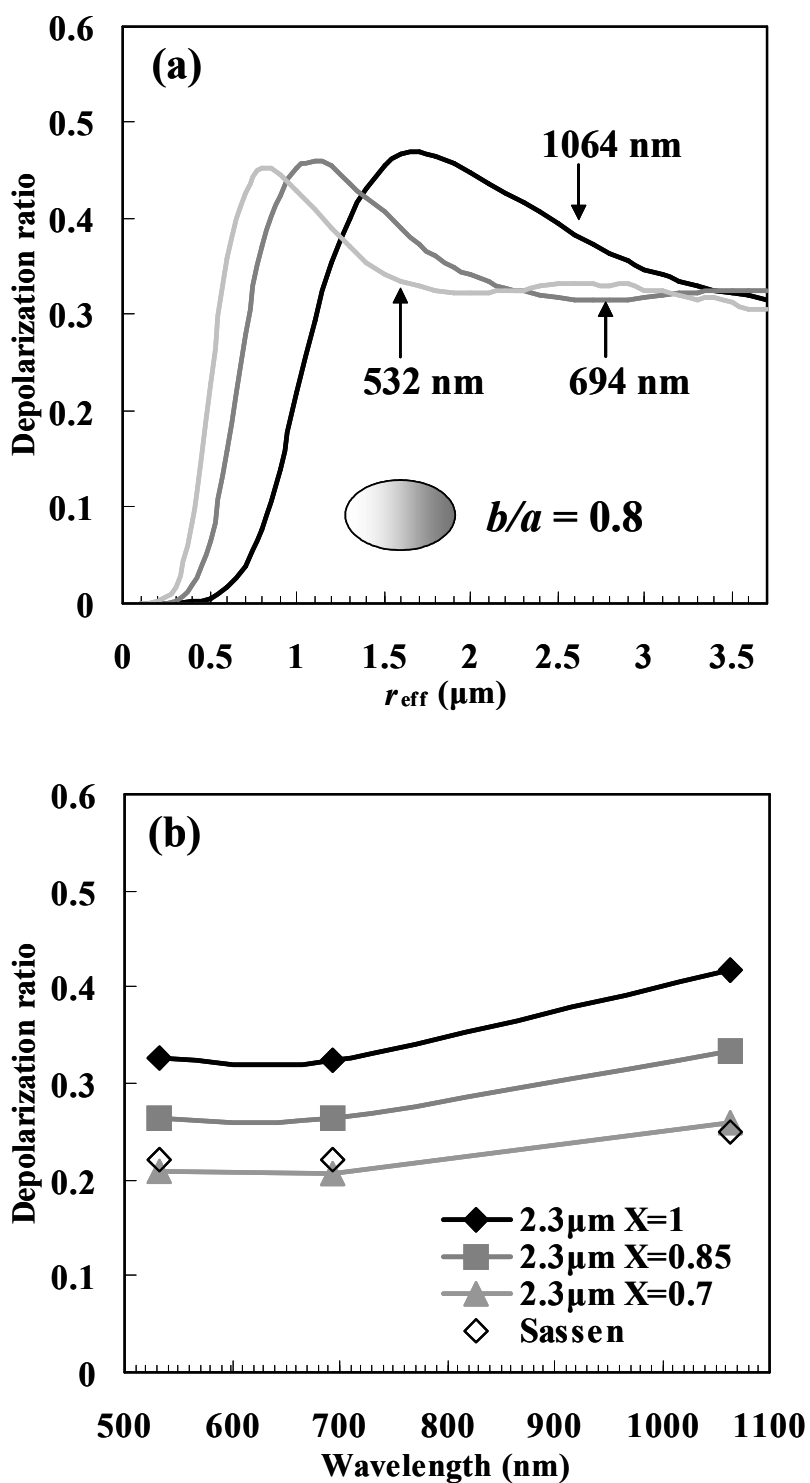
Fig. 6-3. Comparison between observed depolarization ratios by Sassen and calculated depolarization ratios for oblate ice particles with effective radius 2.3 μm on mixing ratio $X = 1$, 0.85, and 0.7. The ◊ symbols indicate the depolarization ratios observed by Sassen et al. (2001).

6.4. Conclusion

We theoretically demonstrated that the use of multi-wavelength depolarization ratios makes possible the characterization of the nonspherical particles using the *T*-matrix computation, the mixing of spherical and nonspherical aerosols also reproduces the existing lidar data. Although this method may not always provide a definitive identification of the shape and size, they can significantly narrow down the plausible range of particle microphysical parameters and can be important in the radiative process related to climate change. Furthermore, although these computations are limited to ice particles, it is applicable to other nonspherical particles such as Asian dust or volcanic ash plume by changing the aspect ratio and the refractive index.

Chapter 7
Noise Reduction in White Light Lidar Signal Based on Wavelet Transform

White light lidar techniques occupy most chapters in this thesis, however signal and image processing concepts are helpful for future discussion toward the IR measurements which the detected white light intensity is expected to be very weak. This chapter presents a brief overview of wavelet denoising.

7.1. Introduction

The multi-wavelength lidar measurements using a coherent white light continuum have the capability of obtaining the wavelength dependence of the backscatter coefficients of aerosols, which can be used to evaluate the particle size distribution (Galvez et al., 2002). However, the present experiment does not fully utilize the potential of a broadband white light continuum. Lidar applications using the infrared region of the white light remain a challenge, because of the rapid decrease of the infrared content of the white light. Furthermore, the transmitted intensity of the white light was very weak for short wavelength (350 nm and 450 nm) as compared with the fundamental wavelength (700 nm and 800 nm). The signals are usually buried in noise, depending on the power of the laser and the observed altitude. In general, the lidar signals with

noise can be improved by moving average method. However, the moving average method only smoothen the signals and does not remove specky values especially the negative values produced by noises (Fang and Huang, 2004).

In this chapter, we propose a method to improve the lidar data by means of 1-D and 2-D wavelet shrinkage. Since the wavelet function is of a localized property, the wavelet transform (WT) has sensitivity to the transient signals such as lidar signal. In addition, since the WT has different resolutions on noise and signal, it can perform denoising process on lidar signal.

7.2. Denoising algorithm

7.2.1. 1-D wavelet shrinkage

In the noise reduction based on WT, we have used the discrete WT (DWT) over the continuous WT (CWT) because CWT is often redundant and computationally expensive. The DWT involves transforming a given signal with wavelet basis functions by dilating and translating it in discrete steps (Daubechies, 1992).

The wavelet shrinkage (Donoho, 1995) is a signal denoising technique based on the idea of thresholding the wavelet coefficients. The wavelet shrinkage can be summarized as follow:

1. Apply the DWT to the signal.
2. Estimate a threshold value.
3. Remove the coefficients that are smaller than the threshold.
4. Perform an inverse DWT and reconstruct the signal.

An algorithm for calculating discrete wavelet decompositions and reconstructions is the Mallat algorithm (Mallat, 1989). The noisy experimental signal $f(t)$ is considered as $s_k^{(0)}$, called a "scaling coefficient" at the 0 level of signal decomposition. Then, as shown in Fig. 7-1, $s^{(j)}$ is successively decomposed into both $s^{(j-1)}$ and $w^{(j-1)}$ by the following formulas:

$$s_k^{(j)} = \sum_n \overline{p_{n-2k}} s_n^{(j-1)} \quad \text{and} \quad w_k^{(j)} = \sum_n \overline{q_{n-2k}} s_n^{(j-1)}, \qquad (7\text{-}1)$$

where $w^{(j)}$ is called the DWT coefficient, $\{p_n\}$ and $\{q_n\}$ are the sequence of coefficient.

$$s_k^{(0)} \longrightarrow s_k^{(1)} \longrightarrow s_k^{(2)} \longrightarrow s_k^{(3)} \cdots$$
$$\searrow \quad \searrow \quad \searrow$$
$$w_k^{(1)} \quad w_k^{(2)} \quad w_k^{(3)} \cdots$$
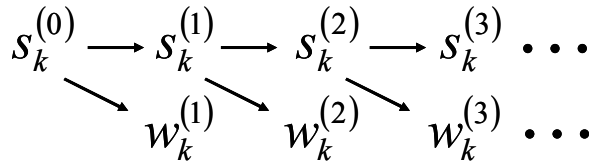
Fig.7-1. 1-D wavelet decomposition.

The sequences p_n of Daubechies' wavelet is given in Table. 7-1. q_n is given by $q_n = (-1)^n p_{1-n}$. We have chosen the Daubechies 5 wavelet which is the most suitable for de-noising the backscattered white light lidar signals (Galvez et al., 2006).

Table 7-1. Daubechies 5 wavelet sequence
Daubechies compactly supported wavelet for N = 5.

N=5
0.1601023979741929
0.6038292697971895
0.7243085284377726
0.1384281459013203
-0.2422948870663823
-0.0322448695846361
0.0775714938400459
-0.0062414902127983
-0.0125807519990820
0.0033357252854738

The level of noise in lidar data is unknown and must be estimated from the noisy data. In this algorithm we have used the universal threshold as suggested in Walczak and Massart (1998),

$$T = \sigma\sqrt{(2\log(N))}, \tag{7-2}$$

where N is the dimensionality of the input data vector and σ is the standard deviation of the noise. The σ is often estimated from the median value of the DWT coefficients at the first level of signal decomposition,

$$\sigma = \frac{\text{Median}\left(\left|w_k^1\right|\right)}{0.6745} \quad \text{(Fang and Huang, 2004)}. \qquad (7\text{-}3)$$

Once the threshold value has been calculated, we can apply a soft threshold to reduce the noise in signal. If the magnitudes of the DWT coefficients, $w_k^{(j)}$, are smaller than this threshold value, the DWT coefficients are replaced by zero, while the rest of them are calculated as $w_k^{(j)}$ $-\ T$. Signal reconstruction can be presented as follows:

$$s_n^{(j-1)} = \sum_k \left[p_{n-2k} s_k^{(j)} + q_{n-2k} w_k^{(j)}\right]. \qquad (7\text{-}4)$$

The denoised signal $s^{(j-1)}$ can be successfully obtained from $w^{(j)}$ and $s^{(j)}$ as shown in Fig. 7-2.

$$\cdots\ s_k^{(3)} \longrightarrow s_k^{(2)} \longrightarrow s_k^{(1)} \longrightarrow s_k^{(0)}$$
$$\cdots\ w_k^{(3)} \qquad w_k^{(2)} \qquad w_k^{(1)}$$
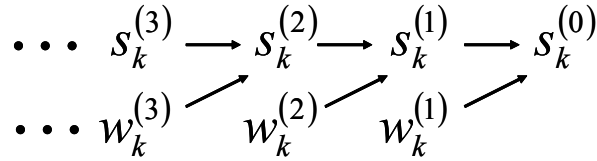
Fig.7-2. 1-D wavelet reconstruction.

7.2.2. 2-D wavelet shrinkage

As shown in Fig. 7-4, the noisy experimental image $f(m,n)$ is considered as $s_{m,n}^{(0)}$ in the same way as 1-D wavelet shrinkage. Then, the algorithm for the computation of the $s_{m,n}^{(j+1)}$ can be summarized by the following four equations:

$$s_{m,n}^{(j+1)} = \sum_l \sum_k \overline{p_{k-2m}}\,\overline{p_{l-2n}}\,s_{k,l}^{(j)}\ ,\quad w_{m,n}^{(j+1,h)} = \sum_l \sum_k \overline{p_{k-2m}}\,\overline{q_{l-2n}}\,s_{k,l}^{(j)}\ ,$$

$$w_{m,n}^{(j+1,v)} = \sum_l \sum_k \overline{q_{k-2m}}\,\overline{p_{l-2n}}\,s_{k,l}^{(j)}\ ,\quad w_{m,n}^{(j+1,d)} = \sum_l \sum_k \overline{q_{k-2m}}\,\overline{q_{l-2n}}\,s_{k,l}^{(j)}\ , \qquad (7\text{-}5)$$

where $w_{m,n}^{(j+1,h)}$ is the coefficient which is applied to the scaling function in the horizontal direction and to the wavelet function in the vertical direction, $w_{m,n}^{(j+1,v)}$ is the coefficient which is applied to the wavelet function in the horizontal direction and to the scaling function in the vertical direction, and $w_{m,n}^{(j+1,d)}$ is the coefficient which is applied to the wavelet function in both directions.
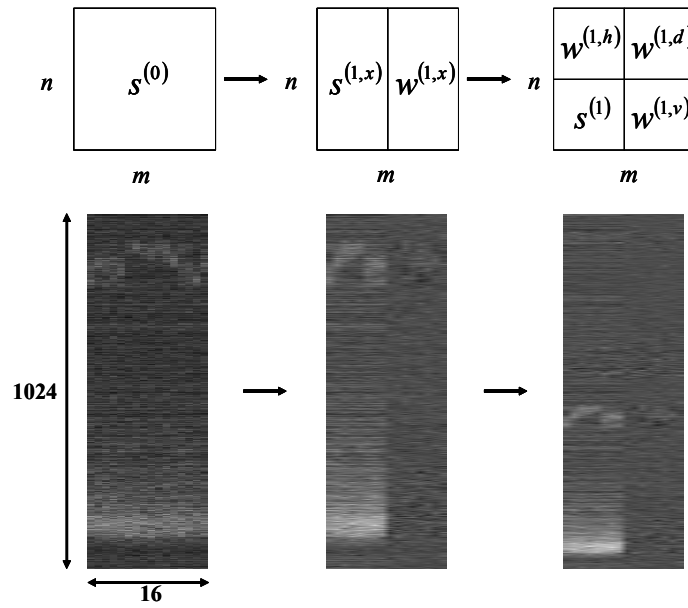
Fig. 7-4. 2-D wavelet transform.

The de-noised image can be reconstructed by

$$s_{m,n}^{(j)} = \sum_k \sum_l \left[p_{m-2k} p_{n-2l} s_{k,l}^{(j+1)} + p_{m-2k} q_{n-2l} w_{k,l}^{(j+1,h)} + q_{m-2k} p_{n-2l} w_{k,l}^{(j+1,v)} + q_{m-2k} q_{n-2l} w_{k,l}^{(j+1,d)} \right].$$

$$(7\text{-}6)$$

7.3. Experimental results and discussion

In this section, we present previous observational results (Somekawa et al., 2006) on the 1-D and 2-D wavelet de-noising algorithms for reducing noise in signal. We have taken a data size of 1024 ($= 2^{10}$) points and decomposed into 10 levels for 1-D and 2-D wavelet denoising.

7.3.1. 1-D wavelet signal denoising

Figure 7-5 shows the denoised lidar signal based on the above 1-D denoising procedure with soft threshold. For comparison, the real signal and moving average signal are presented in Fig. 7-5. In order to check whether our method can filter the noise out and also extract the cloud signals, the relatively noiseless signal at 550 nm where the transmitted white light intensity is intense is also presented in Fig. 7-5(a). Cloud peaks can be seen at about 0.5 km and 1 km. For the strong 550 nm backscattered signals, the wavelets applied for denoising cause no significant difference. However, it can be found that cloud signals which were buried in noise in the weaker channel at 350 nm became noticeable after the denoising procedure by comparing Fig. 7-5(b) with Fig. 7-5(a). Thus, this method can effectively detect the lidar signal buried in noise and reduce noise.
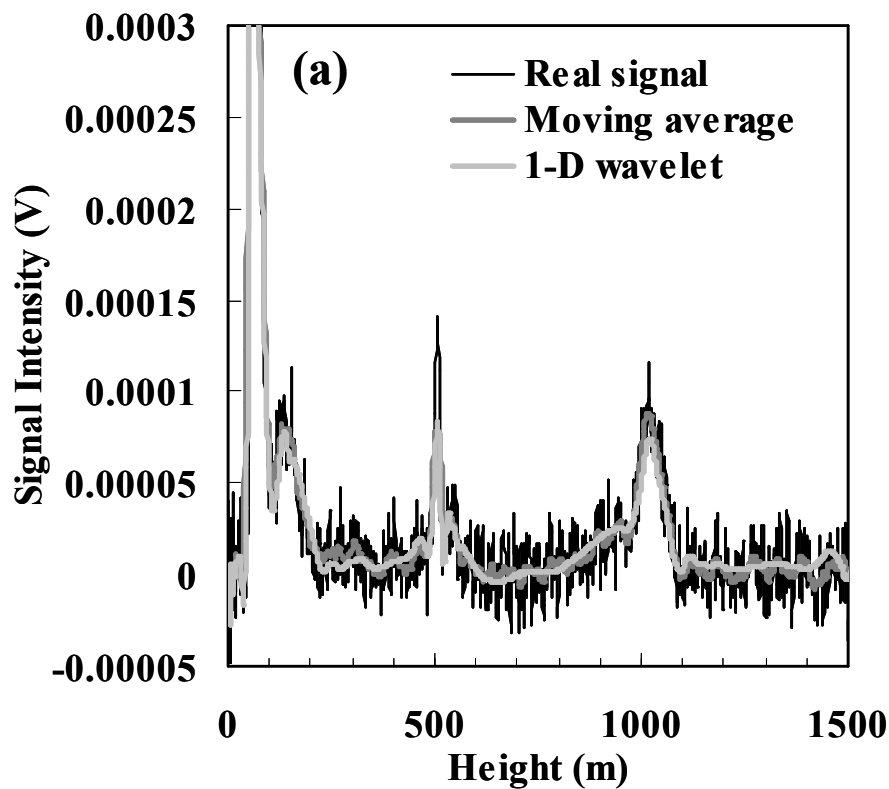
Fig. 7-5. The original liar signal from (a) 550 nm and (b) 350 nm and the corresponding de-noised lidar signals using moving average and 1-D wavelet shrinkage (2005/03/23 2:13).

7.3.2. 2-D wavelet signal denoising

We applied our technique to time height intensity (THI) displays to evaluate the performance of the proposed 2-D method. Since the backscattered lidar signals diminish with the square of the range, the signals were corrected accordingly. This improved to a considerable degree the visualization and interpretation of the obtained lidar signals. The matrix size of the reconstructed THI image is 1024×1024. Assume that the horizontal length of the stored signal dataset is extended to 1024 by repeating the 16-min dataset.

The moving average for range series improves the signal-to-noise ratio and the image quality of experimental lidar THI image especially at 550 nm. But the result of this method still includes the noise. In the moving average THI image at 350 nm, it is not easy to discriminate the high-altitude cloud structures because the noises are generally more pronounces at higher altitude.

As shown in Fig. 7-5(b), the 1-D wavelet denoising images would give improved results. However, the 1-D wavelet denoising images become discontinuous in the horizontal direction because it was applied solely to the intensity level on the vertical line.

The 2-D wavelet denoised images are seen to be smoothed, indicating that the noise has been removed. However, their images exhibit distortions of the boundaries and suffer substantial loss of important detail, especially rapid changes in cloud altitude. During this observation, low-altitude clouds changes at the altitude range 0.5 to 0.6 km, while high-altitude clouds at about 1 km occur at almost the same altitude. In 2-D wavelet denoising, we perform additional horizontal smoothing. As a result, the rapid changes in cloud altitude at 0.5-0.6 km cause a decrease in the signal intensity in the 2-D wavelet images, which give even poorer results. However, in high-altitude clouds, the obtained cloud profiles are slightly improved by reducing the noise around clouds, because the data were not affected by rapid changes of cloud altitude. This seems to be the key feature in 2-D wavelet denoising as compared with the moving average or 1-D wavelet denoising.

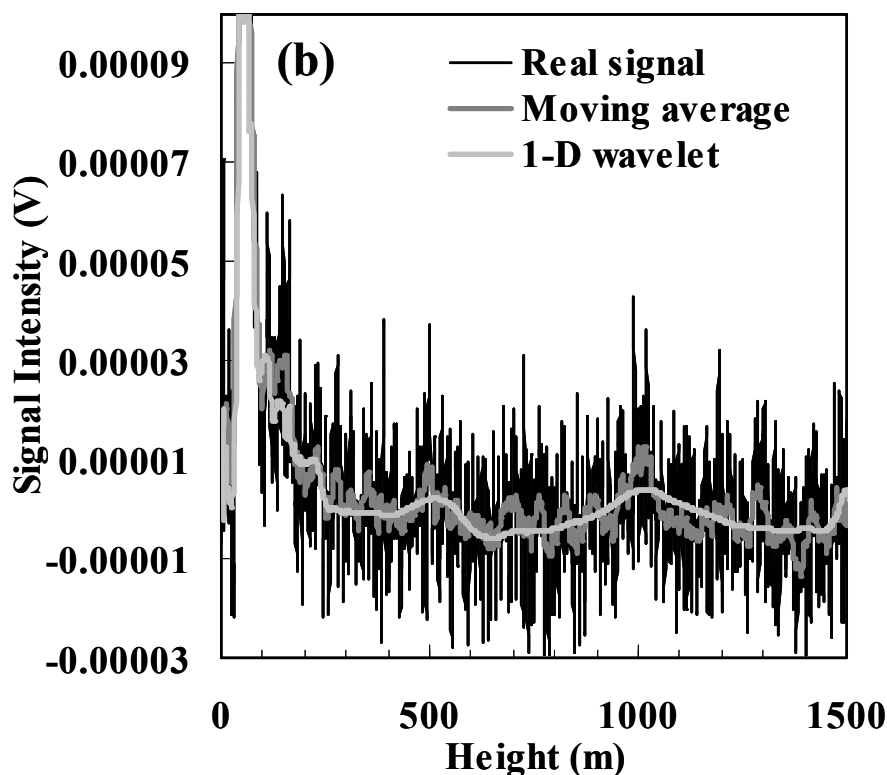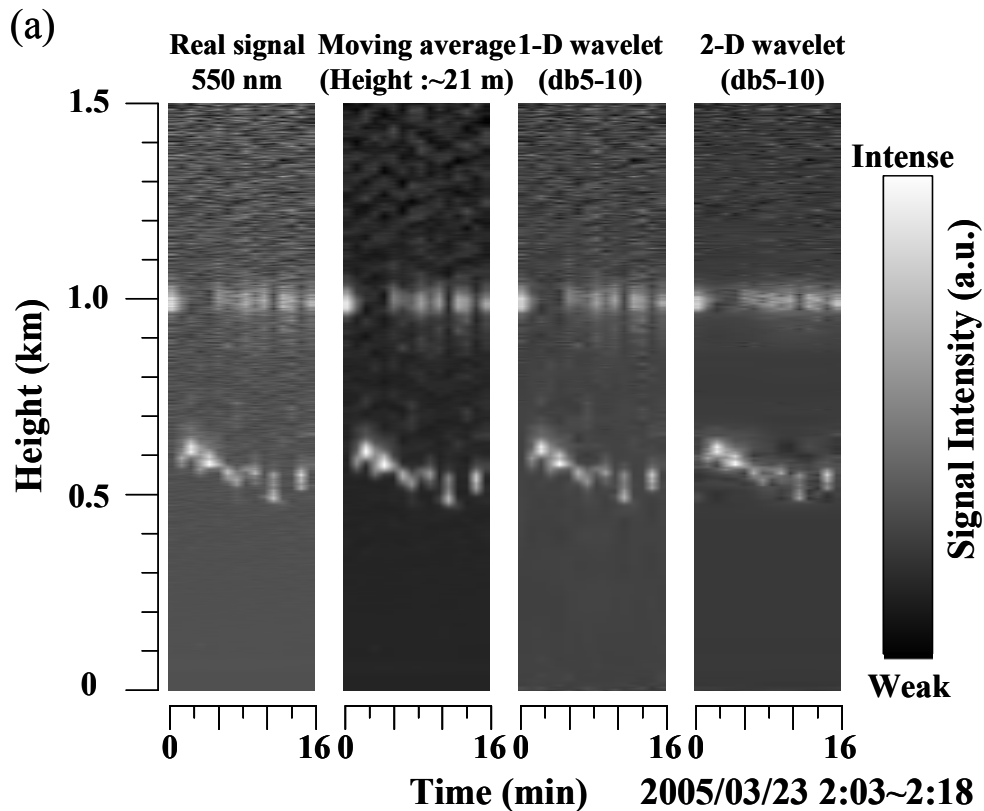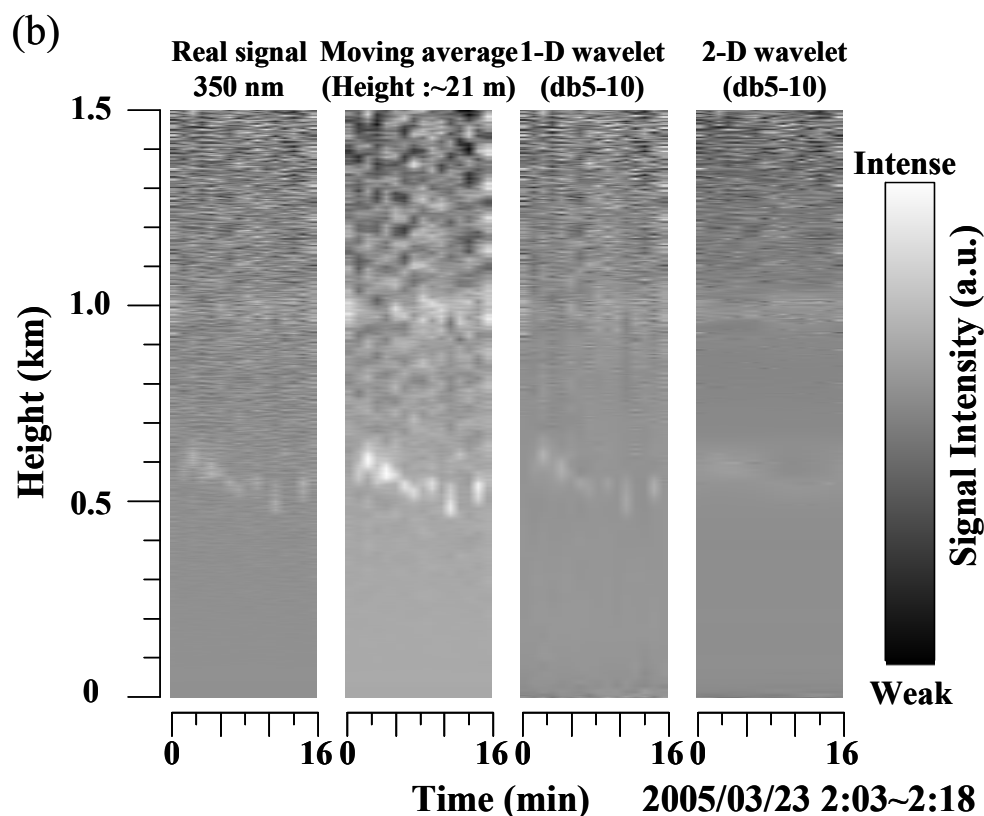Fig. 7-5. The original lidar image from (a) 550 nm and (b) 350 nm and the corresponding de-noised lidar images using moving average, 1-D wavelet shrinkage, and 2-D wavelet shrinkage.

7.4. Conclusion

1-D and 2-D wavelet denoising were applied to white light lidar signals using the Daube-chies 5. Although the wavelet denoising methods cause no significant improvement for strong backscattered signals at 550 nm, they are effective in extracting the signals from the noisy experimental data for the weaker channel at 350 nm. However, wavelet denoising is often inadequate for the rapid changes in cloud altitude when attempting to separate signals from noisy data. Hence, the method needs to be improved to address this situation.

Chapter 8
Summary and Future Prospects

A white light lidar system, which uses self-trapping of the intense femtosecond laser pulse in atmospheric-pressure Kr gas, was utilized to obtain multi-wavelength backscatter and depolarization profiles from aerosols and clouds. The white light lidar has the advantage of performing at an arbitrary wavelength that is independent of the laser source. The research reported in this thesis describes the first use, as far as we know, of the coherent white light continuum for the depolarization remote sensing. The white light depolarization lidar system permits expanded studies to estimate the shape of clouds and aerosols. These results may be an important step in future studies to solve the not-yet-understood mechanisms for generating the coherent white light continuum or the physics of beam propagation of femtosecond laser pulse in atmosphere.

In chapter 2, the initial experiments were described to provide a proof-of-principle that the white light depolarization lidar works, and that results correspond with more traditional measurement techniques. The motivation for the development of white light lidar systems with depolarization detection capabilities is their use for the multi-wavelength depolarization lidar. In addition, the properties of the white light continuum generated in Kr gas were investigated. White light generated from Kr gas is polarized in the same direction as the incident laser polarization. Recently, various polarization dependences of the white light have been observed, such as conversion efficiency enhancement for circular polarization (Yang et al., 2005) and depolarization of white light generated in BK7 glass (Dharmadhikari et al., 2006). These results make the white light depolarization techniques more manageable. Thus, applications of this white light would have spread widely to include femtosecond time-resolved spectroscopy (e.g., chan-

neled spectroscopic polarimetry (Oka and Kato, 1999)) as well as remote sensing.

The obtained depolarization ratios show the wavelength dependence, our white light lidar system was extended to simultaneous three-wavelength depolarization lidar system as shown in chapter 3. By using the three-wavelength depolarization ratio, which is obtained without any complex inversion algorithm, we can observe the characteristics of aerosols and clouds. We also evaluated the size of the particles in cloud layers by calculating the depolarization based on *T*-matrix method and comparing them with the Angstrom coefficients. In development of the next stage of the depolarization lidar such as the four Stokes vector measurements (Houston and Carswell, 1978), recent progress in the development of actively controlled liquid crystal ratarders has made measurement of the complete polarization relatively simple (Guasta et al., 2006; Flynn et al., 2007). This has the advantage of requiring fewer receiver components and offering simpler single-detection calibration.

In chapter 4, the Asian dust observations were introduced as a real example of environmental applications using the white light lidar system. We can clearly see the indication of Asian dust events; the depolarization ratio became higher than the usual value of ~0. Although preliminary, they open the way to a depolarization analysis of the Asian dust. Further, accumulation of observations is indispensable to clarify the depolarization property of the Asian dust.

For backscatter lidar, multiple scattering offers new possibilities. The depolarization ratios by the multiple-FOV measurements were discussed in chapter 5. This chapter shows that the wavelength dependence of multiply scattered lidar returns may contain retrievable information on cloud parameter such as optical depth and droplet size. We observed the possibility that the depolarization ratio of the multiple scattering can provide some relevant parameters.

A detailed analysis of the *T*-matrix computation in chapter 3 is described in chapter 6. This chapter gives a more detailed description of the *T*-matrix computation and also shows the evaluations of other particle shape or the mixing of spherical and nonspherical particles. Other favored crystal shapes, which have not been attempted in this thesis in detail, may lead to the more promising agreement between measured and calculated depolarization ratio.

In chapter 7, we report on the wavelet denoising toward developing a technique for remotely analyzing simultaneous range-resolved multi-trace gas using the IR side of the coherent white light continuum. Our denoising results show that most of the noise in the weak signal regime is removed by the proposed method and the signals from clouds and aerosols preserved

well. This result showed that the wavelet signal denoising can improve the detectable range of the white light lidar system.

Bibliography

Ackermann R., Mejean G., Kasparian J., Yu J., Salmon E. and Wolf J. -P., Laser filaments generated and transmitted in highly turbulent air, *Opt. Lett.*, **31**, 86-88, 2006.

Althanusen D., Muller D., Ansmann A., Wandinger U., Hube H., Clauder E. and Zorner S., Scanning 6-wavelength 11-channel aerosol lidar, *J. Atmos. Ocean. Technol.*, **17**, 1469-1482, 2000.

Bissonnette L. R. and Roy G., Range-height scans of lidar depolarization for characterizing properties and phase of clouds and precipitation, *J. Atmos. Ocean. Technol.*, **18**, 1429-1446, 2001.

Bourayou R., Mejean G., Kasparian J., Rodriguez M., Salmon E., Yu J., Lehmann H., Stecklum B., Laux U., Eisloffel J., Scholz A., Hatzes A. P., Saurebrey R., Woste L. and Wolf J. P., White-light filaments for multiparameter analysis of cloud microphysics, *J. Opt. Soc. Am. B*, **22**, 369-377, 2005.

Boutou V., Favre C., Woeste L. and Wolf J. -P., Measuring the electric charge in cloud droplets by use of second-harmonic generation, *Opt. Lett.*, **30**, 759-761, 2005.

Brodeur A. and Chin S. L., Band-gap dependence of the ultrafast white-light continuum, *Phys. Rev. Lett.*, **80**, 4406-4409, 1998.

Browell E. V., Butler C. F., Ismail S., Robinette P. A., Carter A. F., Higdon N. S., Toon O. B., Schoeberl M. R. and Tuck A. F., Airborne lidar observations in the wintertime arctic stratosphere: Polar stratospheric clouds, *Geophys. Res. Lett.*, **17**, 385-388, 1990.

Chui C.K., An introduction to wavelets: Wavelet Analysis and its Applications, volume 1. (Academic Press, Boston, 1992).

Close D. H., Giuliano C. R., Hellwarth R. W., Hess L. D., Mcclung F. J. and Wagner W. G., The self-focusing of light of different polarizations, *IEEE J. Quant. Electron.*, **QE-2**, 553-557, 1966.

Collis R. T. H. and Russell P. B., "Lidar measurement of particles and gases by elastic backscat-tering and differential absorption," in Laser Monitoring of the Atmosphere, E. D. Hinkley, Ed. (Springer, New York 1976), Chap. 4.

Daubechies I., Ten Lectures on Wavelet (SIAM, Philadelphia, PA, 1992).

Dharmadhikari A. K., Rajgara F. A. and Mathur D., Depolarization of white light generated by ultrashort laser pulses in optical media, *Opt. Lett.*, **31**, 2184-2186, 2006.

Donoho D. L., De-Noising by Soft-Thresholding, *IEEE Trans. Inform. Theory*, **41**, 613-627, 1995.

Eck T. F., Holben B. N., Reid J. S., Dubovik O., Smirnov A., O'Neil N. T., Slutsker I. and Kinne S., Wavelength dependence of the optical depth of biomass burning, urban, and desert dust aerosols, *J. Geophys. Res.*, **104**, 31,333-31,349, 1999.

Fang H. T. and Huang D. S., Noise reduction in lidar signal based on discrete wavelet transform, *Opt. Commun.*, **233**, 67-76, 2004.

Fernald F. G., Analysis of atmosphere lidar observations: some comments, *Appl. Opt.*, **23**, 652-63, 1984.

Flynn C. J., Mendoza A., Zheng Y. and Mathur S., Novel polarization-sensitive micropulse lidar measurement technique, *Opt. Express*, **15**, 2785-2790, 2007.

Fujii T., Goto N., Miki M., Nayuki T. and Nemoto K., Lidar measurement of constituents of mircoparticles in air by laser-induced breakdown spectroscopy using femtosecond tera-watt laser pulses, *Opt. Lett.*, **31**, 3456-3458, 2006.

Galvez M. C., Fujita M., Inoue N., Moriki R., Izawa Y. and Yamanaka C., Three-wavelength backscatter measurement of clouds and aerosols using a white light lidar system, *Jpn. J. Appl. Phys.*, **41**, L284-L286, 2002.

Galvez M. C., Somekawa T., Yamanaka C. and Fujita M., Wavelet denoising applied to multi-wavelength depolarization white light lidar measurement, *Proc. 23rd International Laser Radar Conference*, 275-278, 2006.

Guasta M. D., Valler E., Riviere O., Castagnoli F., Venturi V. and Morandi M., Use of polarimetric lidar for the study of oriented ice plate in clouds, *Appl. Opt.*, **45**, 4878-4887, 2006.

Hayashida S. and Horikawa M., Anti-correlation between stratospheric aerosol extinction and the Angstrom parameter from multiple wavelength measurements with SAGA II – a characteristic of the decay period following major volcanic eruptions, *Geophys. Res. Lett.*, **28**, 4063-4066, 2001.

Houston J. D. and Carswell A. I., Four-component polarization measurement of lidar atmospheric scattering, *Appl. Opt.*, **17**, 614-620, 1978.

Hu Y., Liu A., Winker D., Vaughan M. and Noel V., Simple relation between lidar multiple scattering and depolarization for water clouds, *Opt. Lett.*, **31**, 1809-1811, 2006.

Iwasaka Y., Shibata T., Nagatani T., Shi G. -Y., Kim Y. S., Matsuki A., Trochkine D., Zhang D., Yamada M., Nagatani M., Nakata H., Shen Z., Li G., Chen B. and Kawahira K., Large depolarization ratio of free tropospheric aerosols over the Taklamakan Desert revealed by lidar measurements: Possible diffusion and transport of dust particles, *J. Geophys. Res.*, **108**, 8652, 2003.

Kasparian J., Sauerbrey R., Mondelain D., Nidermeier S., Yu J., Wolf J. P., Andre Y. B., Franco M., Prade B., Tzortzakis S., Mysyrowicz A., Rodriguez M., Wille H. and Woste L., Infrared extension of the supercontinuum generated by femtosecond terawatt laser pulses propagating in the atmosphere, *Opt. Lett.*, **25**, 1397-1399, 2000.

Kasparian J., Rodriguez M., Mejean G., Yu J., Salmon E., Wille H., Bourayou R., Frey S., Andre Y. B., Mysyrowicz A., Sauerbrey R., Wolf J. P. and Woste L., White-light filaments for atmospheric analysis, *Science*, **301**, 61-64, 2003.

Kim K. -H., Choi G. -H., Kang C. -H., Lee J. -H., Kim J. Y., Youn Y. H. and Lee S. R., The chemical composition of fine and coarse particles in relation with the Asian Dust events, *Atmos. Environ.*, **37**, 753-765, 2003.

Klimov V. I. and McBranch D.W, Femtosecond high-sensitivity, chirp-free transient absorption spectroscopy using kilohertz lasers, *Opt. Lett.*, **23**, 277-279, 1998.

Kovalenko S. A., Dobryakov A. L. Ruthmann J. and Ernsting N. P., Femtosecond spectroscopy

of condensed phases with chirped supercontinuum probing, *Phys. Rev. A*, **59**, 2369-2384, 1999.

Mallat S., A Theory for Multiresolution Signal Decomposition: The Wavelet Representation, *IEEE Trans. Pattern Anal.*, **11**, 674-693, 1989.

Mechain G., Mejean G., Ackermann R., Rohwetter P., Andre Y. -B., Kasparian J., Prade B., Stelmaszczyk K., Yu J., Salmon E., Winn W., Schlie L. A. (Vern), Mysyrowicz A., Sauerbrey R., Woste L. and Wolf J. -P., Propagation of fs TW laser filaments in adverse atmosphere conditions, *Appl. Phys. B* **80**, 785-789, 2005.

Mejean G., Kasparian J., Salmon E., Yu J., Wolf J. P., Bourayou R., Sauerbrey R., Rodriguez M., Woste L., Lehmann H., Stecklum B., Lauw U., Eisloffel J., Scholz A. and Hatzes A. P., Towards a supercontinuum-based infrared lidar, *Appl. Phys. B* **77**, 357-359, 2003.

Mejean G., Kasparian J., Yu J., Frey S., Salmon E. and Wolf J. P., Remote detection and identification of biological aerosols using a femtosecond terawatt lidar system, *Appl. Phys. B* **78**, 535-537, 2004.

Mejean G., Kasparian J., Yu J., Salmon E., Wolf J. -P., Skupin S., Vincotte A., Nulter R., Champeaux S. and Berge L., Multifilamentation transmission through fog, *Phys. Rev. E* **72**, 026611, 2005

Midorikawa K., Kawano H., Suda A., Nagura C. and Obara M., Polarization properties of ultrafast white-light continuum generated in condensed media, *Appl. Phys. B* **78**, 535-537, 2004.

Mishchenko M. I., Travis L. D., Kahn R. A. and West R. A., Modeling phase function for dustlike tropospheric aerosols using a shape mixture of randomly oriented polydisperse spheroids, *J. Geophys. Res.*, **102**, 16,831-16,847, 1997.

Mishchenko M. I., Sassen K., Depolarization of lidar returns by small ice crystals: an application to contrails, *Geophys. Res. Lett.*, **25**, 309-312, 1998.

Mishchenko M. I. and Travis L. D., Capabilities and Limitations of a Current Fortran Implementation of the T-matrix Method for Randomly Oriented, Rotationally Symmetric Scat-

terers. *J. Quant. Spectrosc. Radiat. Transfer.*, **60**, 309-324, 1998.

Mori I., Iwasaka Y., Matsunaga K., Hayashi M. and Nishikawa M., Chemical characteristics of free tropospheric aerosols over the Japan Sea coast: aircraft-borne measurements, *Atmos. Environ.*, **33**, 601-609, 1999.

Murayama T., Okamoto H., Kaneyasu N., Kamataki H. and Miura K., Application of lidar depolarization measurement in the atmospheric boundary layer: Effects of dust and sea-salt particles, *J. Geophys. Res.*, **104**, 31,781-31,792, 1999.

Murayama T., Sugimoto N., Uno I., Kinoshita K., Aoki K., Hagiwara N., Liu Z., Matsui I., Sakai T., Shibata T., Arao K., Sohn B. -J., Won J. -G, Yoon S. -C., Li T., Zhou J., Hu H., Abo M., Iokibe K., Koga R. and Iwasaka Y., Ground-based network observation of Asian dust events of April 1998 in east Asia, *J. Geophys. Res.*, **106,** 18,345-18,359, 2001.

Murayama T., Muller D., Wada K., Shimizu A., Sekiguchi M. and Tsukamoto T., Characterization of Asian dust and Siberian smoke with multi-wavelength Raman lidar over Tokyo, Japan in spring 2003, *Geophys. Res. Lett.*, **31**, L23103, 2004.

Nakajima T., King M. D., Spinhirne J. D. and Radke L. F., Detection of the optical thickness and effective particle radius of clouds from reflected solar radiation measurements. Part II: Marine stratocumulus observations, *J. Atmos. Sci.*, **48**, 728-750, 1991.

Nishioka H., Odajima W., Ueda K. and Takuma H., Ultrabroadband flat continuum generation in multichannel propagation of terrawatt Ti:sapphire laser pulses, *Opt. Lett.*, **20**, 2505-2507, 1995.

Nishioka H. and Ueda K. -I., Super-broadband continuum generation with transient self-focusing of a terawatt laser pulse in rare gases, *Appl. Phys. B* **77**, 171-175, 2003.

Oka K., Kato T., Spectroscopic polarimetry with a channeled spectrum, *Opt. Lett.*, **24**, 1475-1477, 1999.

Pal S. R. and Carswell A. I., Polarization properties of lidar backscattering from clouds, *Appl. Opt.*, **12**, 1530-1535, 1973.

Pal S. R. and Carswell A. I., Polarization properties of lidar scattering from clouds at 347 nm

and 694 nm, *Appl. Opt.*, **17**, 2321-2328, 1978.

Pruppacher H. R. and Klett J. D., Microphysics of Clouds and Precipitation, 2nd rev. and enl. ed. (Kluwer academic, Dordrecht, 1997**)** p. 42.

Rairoux P., Schillinger H., Niedermeier S., Rodriguez M., Ronneberger F., Suerbrey H., Stein B., Waite D., Wedeking C., Wille H., Woste L. and Ziener C., Remote sensing of the atmosphere using ultrashort laser pulses, *Appl. Phys. B* **71**, 573-580, 2000.

Ranka J. K., Schirmer R. W. and Gaeta A. L., Observation of pulse splitting in nonlinear dispersive media, *Phys. Rev. Lett.*, **77**, 3783-3786, 1996.

Reichardt S., Reichardt J., Effect of multiple scattering on depolarization measurements with spaceborne lidars, *Appl. Opt.*, **42**, 3620-3633, 2003.

Roy G., Bissonnette L., Bastille C. and Vallee G., Retrieval of Droplet-size Density Distribution from Multiple-field-of-view Cross-polarized Lidar Signals: Theory and Experimental Validation. *Appl. Opt.*, **38**, 5202-5211, 1999.

Sasano Y. and Browell E. V., Light scattering characteristics of various aerosol type derived from multiple wavelength lidar observations, *Appl. Opt.*, **28**, 1670-1679, 1989.

Sassen K., Huggins A. W., Long A. B., Snider J. B. and Meitin R. J., Investigations of a winter mountain storm in Utah. Part II: Mesoscale structure, supercooled liquid water development, and precipitation processes, *J. Atmos. Sci.* **47**, 1323-1350, 1990

Sassen, K., The polarization lidar technique for cloud research: a review and current assessment, *Bull. Am. Meteorol. Soc.*, **72**, 1848-1866, 1991.

Sassen K. and Zhao H., Lidar multiple scattering in water droplet clouds: Toward an improved treatment, *Opt. Rev.*, **5**, 394-400, 1995.

Sassen K., Comstock J. M., Wang Z. and Mace G. G., Cloud and Aerosol Research Capabilities at FARS: The Facility for Atmospheric Remote Sensing, *Bull. Am. Meteorol. Soc.*, **82** 1119-1138, 2001.

Sassen K., Indirect climate forcing over the western US from Asian dust storms, *Geophys. Res.*

Lett., **29**, 1465, 2002.

Shen Y. R., The Principle of Nonlinear Optics (J. Wiley, New York, 1984).

Shimizu A., Sugimoto N., Matsui I., Arao K., Uno I., Murayama T., Kagawa N., Aoki K., Uchiyama A. and Yamazaki A., Continuous observations of Asian dust and other aerosols by polarization lidars in China and Japan during ACE-Asia, *J. Geophys. Res*., **109**, D19S17, doi: 10.1029/2002JD003253, 2004.

Somekawa T., Yamanaka C., Fujita M. and Galvez M. C., Depolarization light detection and ranging using a white light lidar system, *Jpn. J. Appl. Phys*., **45**, L165-L168, 2006.

Somekawa T., Yamanaka C., Fujita M. and Galvez M. C., Simultaneous three-wavelength depolarization measurement of clouds and aerosols using a coherent white light continuum, *J. Appl. Phys*., 103, 043101, 2008.

Srivastava A. and Goswami D., Control of supercontinuum generation with polarization of incident laser pulses, *Appl. Phys. B* **77**, 325-328, 2003.

Stefanutti L., Castagnoli F., Guasta M. D., Morandi M., Sacco V. M., Venturi V., Zuccagnoli L., Kolenda J., Kneipp H.,, Rairoux P., Stein B., Weidauer D. and Wolf J. P., A four-wavelength depolarization backscattering lidar for polar stratospheric cloud monitoring, *Appl. Phys. B* **55**, 13-17, 1992.

Stelmaszczyk K., Rohwetter P., Mejean G., Yu J., Salmon E., Kasparian J., Ackermann R., Wolf J. -P. and Woste L., Long-distance remote laser-induced breakdown spectroscopy using filamentation in air, *Appl. Phys. Lett.*, **85**, 3977-3979, 2004.

Sugimoto N. and Lee C. H., Characteristics of Dust Aerosols Inferred from Lidar Depolarization Measurements at Two Wavelengths. *Appl. Opt*., **45**, 7468-7474, 2006.

Tatarov B., Trifonov T., Kaprielov B. and I. Kolev, Dependence of the lidar signal depolarization on the receiver's field of view in the sounding of fog and clouds, *Appl. Phys. B* **71** , 593-600, 2000.

Tatarov B. and Sugimoto N., Estimation of quartz concentration in the tropospheric mineral

aerosols using combined Raman and high-spectral-resolution lidars, *Opt. Lett.*, **30**, 3407-3409, 2005.

Tegen I., Lacis A. A. and Fung I., The influence on climate forcing of mineral aerosols from disturbed soils, *Nature*, **380**, 419-422, 1996.

Toon O. B., Browell E. V., Kinne S. and Jordan J., An analysis of lidar observations of polar stratospheric clouds, *Geophys. Res. Lett.*, **17**, 393-396, 1990.

Uno I., Carmichael G. R., Streets D. G., Tang Y., Yienger J. J., Satake S., Wang Z., Woo Jung-Hun, Guttikunda S., Uematsu M., Matsumoto K., Tanimoto H., Yoshioka K. and Iida T., Regional chemical weather forecasting system CFORS: Model descriptions and analysis of surface observations at Japanese island stations during the ACE-Asia experiment, *J. Geophys. Res.*, **108**, 8668, 2003.

Var F., Narita Y. and Tanaka S., The concentration, trend and seasonal variation of metals in the atmosphere in 16 Japanese cities shown by the results of National Air Surveillance Network (NASN) from 1974 to 1996, *Atmos. Environ.*, **34**, 2755-2770, 2000.

Walczak B. and Massart L., Noise suppression and signal compression using the wavelet packet transform, *Chemom. Intel. Lab. Syst.*, **36**, 81-94, 1998.

Wang Q., Schoenlein R. W., Peteanu L. A. and Mathies R. A., Vibrationally coherent photochemistry in the femtosecond primary event of vision, *Science*, **266**, 422-424, 1994.

Warren S. G., Optical Constants of Ice from the Ultraviolet to the Microwave. *Appl. Opt.*, **23**, 1206-1225, 1984.

Weitkamp C, ed., Lidar: range-resolved optical remote sensing of the atmosphere (Springer, 2005).

Whiteman D. N. and Melfi S. H., Cloud Liquid Water, Mean Droplet Radius, and Number Density Measurements Using a Raman Lidar. *J. Geophys. Res.*, **104**, 31,411-31,419, 1999.

Yang H., Zhang J., Zhang Q., Hao Z., Li Y., Zheng Z., Wang Z., Dong Q., Lu X., Wei Z., Sheng Z., Yu J. and Yu W., Polarization-dependent supercontinuum generation from light fila-

ments in air, *Opt. Lett*., **30**, 534-536, 2005.

Yu J., Mondelain D., Ange G., Volk R., Niedermeier S., Wolf J. P., Kasparian J. and Sauerbrey R., Backward supercontinuum emission from a filament generated by ultrashort laser pulses in air, *Opt. Lett*., **26**, 533-535, 2001.

List of Publications and Presentations

Publications

1. C. Yamanaka, T. Somekawa, M. Fujita, C. Yamanaka, M. C. D. Galvez, E. A. Vallar, Y. Takeuchi, Y. Izawa, Multi-Wavelength Backscatter Measurements of Clouds and Aerosols Using a White Light LIDAR System, Proceedings of the 7th International Congress on Optical Particle Characterization, pp381-386, 2006.

2. T. Somekawa, C. Yamanaka, M. Fujita and M. C. Galvez, Depolarization Lidar Measurements Using a Coherent White Light Continuum, 13th Coherent Laser Radar Conference Proceedings, pp 96-99, 2005.

3. T. Somekawa, C. Yamanaka, M. Fujita and M. C. Galvez, Depolarization Light Detection and Ranging Using a White Light LIDAR System, Jpn. J. Appl. Phys, The Japan Society of Applied Physics, **45**, No6, pp L165-L168, 2006.

4. T. Somekawa, C. Yamanaka, M. Fujita and M. C. Galvez, Towards a Multi-wavelength Depolarization Lidar Using a Coherent White Light Continuum, Reviewed and revised papers presented at the 23rd International Laser Radar Conference, The Conference Steering Committee of the 23rd ILRC, Part 1, pp253-256, 2006.

5. M. C. Galvez, T. Somekawa, C. Yamanaka and M. Fujita, Wavelet Signal Denoising Applied to Multiwavelength-Depolarization White Light Lidar Measurement, Reviewed and revised papers presented at the 23rd International Laser Radar Conference, The Conference Steering Committee of the 23rd ILRC, Part 1, pp275-278, 2006.

6. M. C. D. Galvez, E. A. Vallar, T. Somekawa, C. Yamanaka, Y. Izawa and M. Fujita, A White Light LIDAR for Multi-wavelength Depolarization Measurement, Proceedings of the Seventh OU-DLSU Academic Research Workshop, Judeaus Printing Service, pp60-63, 2006.

7. C. Yamanaka, T. Somekawa, M. Fujita and M. C. Galvez, Simultaneous Three-Wavelength Depolarization Measurement Using a White Light System, International Workshop 2007, The 21st century COE Program "Towards a New Basic Science: Depth and Synthesis", pp101, 2007.

8. T. Somekawa, C. Yamanaka, M. Fujita and M. C. Galvez, A New Concept to Characterize Nonspherical Particles from Multi-wavelength Depolarization Ratios Based on *T*-matrix Computation, Part. Part. Syst. Charact., WILEY-VCH, **25**, pp 49-53, 2008.

9. T. Somekawa, C. Yamanaka, M. Fujita and M. C. Galvez, Simultaneous three-wavelength depolarization measurement of clouds and aerosols using a coherent white light continuum,

J. Appl. Phys., **103**, 043101, 2008.

10. T. Somekawa, C. Yamanaka, M. Fujita and M. C. Galvez, Observation of Asian Dust Aerosols with Depolarization Lidar Using a Coherent White Light Continuum, Jpn. J. Appl. Phys, The Japan Society of Applied Physics, accepted.

11. T. Somekawa, C. Yamanaka, M. Fujita and M. C. Galvez, Dependence of the multiple scattering depolarization on the wavelength using the white light lidar system, Opt. Lett., Optical Society of America, submitted.

Japanese articles

1. 染川智弘、池谷元伺, 「トルコ地震に伴う「モーゼ現象」の再現模型実験」、『マテリアルインテグレーション』、（株)TIC、17 巻、11 号, pp 61-64, 2004

2. 染川智弘、山中千博、藤田雅之、M. C. Galvez、「コヒーレント白色光を用いた偏光ライダー‐3 波長同時偏光解消度観測とウェーブレット縮退によるノイズ除去‐」、『レーザー学会　第356回研究会報告　21世紀のレーザー技術』、社団法人　レーザー学会、RTM-06-49、pp13-18、2006 年 11 月

Presentations

-International Symposium-

Oral Presentations

1. T. Somekawa, C. Yamanaka, M. Fujita and M. C. Galvez, Depolarization Lidar Measurements Using a Coherent White Light Continuum, The 13th Coherent Laser Radar Conference, pp 96-99, Kamakura, Japan, (October 2005)

2. T. Somekawa, C. Yamanaka, M. Fujita and M. C. Galvez, Simultaneous Three-Wavelength Depolarization Measurement Using a White Light Lidar System, 8th International Congress on Optical Particle Characterization, Graz, Austria, (July 2007)

Poster Presentations

1. Yamanaka, C., Somekawa, T., Fujita, M., Yamanaka, C., Takeuchi, Y., Izawa, Y., M, C, Galvez., E, A, Vallar, Multi-Wavelength Backscatter Measurements of Clouds and Aerosols Using a White Light LIDAR System, 7th International Congress on Optical Particle Characterization, P-11, Kyoto, Japan, (August 2004)

2. T. Somekawa, C. Yamanaka, M. Fujita and M. C. Galvez, Towards a Multi-wavelength Depolarization Lidar Using a Coherent White Light Continuum, The 23rd International

Laser Radar Conference, 2P-53, Nara , Japan, (July 2006)

3. M. C. Galvez, T. Somekawa, C. Yamanaka and M. Fujita, Wavelet Signal Denoising Applied to Multiwavelength-Depolarization White Light Lidar Measurement , The 23rd International Laser Radar Conference, 2P-59, Nara, Japan, (July 2006)

4. T. Somekawa, C. Yamanaka, M. Fujita and M. C. Galvez, Simultaneous three-wavelength depolarization Lidar using a coherent white light continuum, The CLEO/Europe-IQEC Conference, CH-2-MON, ICM Munich , Germany, (June 2007)

5. C. Yamanaka, T. Somekawa, M. Fujita and M. C. Galvez, Simultaneous Three-Wavelength Depolarization Measurement Using a White Light System, International Workshop 2007, The 21st century COE Program "Towards a New Basic Science: Depth and Synthesis", PP3, Osaka University, Japan, (September 2007)

-Domestic Symposium-

Oral Presentations

1. 山中千博、染川智弘、藤田雅之、 「コヒーレント白色光を用いた環境計測の基礎実験」、『平成 16 年春季　第 51 回応用物理学関係連合講演会』、28p-ZA-9、東京工科大学、2004 年 3 月

2. 山中千博、染川智弘、藤田雅之、「コヒーレント白色光を用いた環境計測の基礎実験」、『平成 16 年秋季　第 65 回応用物理学会学術講演会』、4p-ZD-7、東北学院大学、2004 年 9 月

3. 染川智弘、山中千博、藤田雅之、M. C. Galvez、「コヒーレント白色光を用いた 5 波長偏光解消ライダー」、『平成 17 年秋季　第 66 回応用物理学会学術講演会』、7p-H-5、徳島大学,2005 年 9 月

4. 染川智弘、山中千博、藤田雅之、「コヒーレント白色光を用いた 3 波長同時偏光解消ライダー」、 『平成 18 年秋季　第 67 回応用物理学会学術講演会』、1a-ZA-7、立命館大学、2006 年 9 月

5. 染川智弘、山中千博、藤田雅之、M. C. Galvez、「コヒーレント白色光を用いた偏光ライダー‐3 波長同時偏光解消度観測とウェーブレット縮退によるノイズ除去‐」、『レーザー学会　第 356 回研究会報告　21 世紀のレーザー技術』、RTM-06-49、徳島大学、 2006 年 12 月

6. 染川智弘、山中千博、藤田雅之, M. C. Galvez、「コヒーレント白色光を用いた偏光ライダー」、『レーザー学会学術講演会第 27 回年次大会』、E6-18pV7、 宮崎市フェニックスシーガイアリゾート、2007 年 1 月

7. 染川智弘、山中千博、藤田雅之、「白色光偏向ライダーによる雲・エアロゾルの 3 波長同時偏光解消度観測」、『平成 19 年春季　第 54 回応用物理学関係連合講演会』、

28p-SJ-6、青山学院大学、 2007 年 3 月

8. 染川智弘、山中千博、藤田雅之、「白色光ライダーによる粒径分布の測定と黄砂の観測」、 『平成 19 年秋季 第 68 回応用物理学会学術講演会』、7p-ZA-9、北海道工業大学、2007 年 9 月

Poster Presentations

1. 染川智弘、池谷元伺、「トルコ地震の前の「モーゼ現象」」、『日本地震学会』、P149、パシフィコ横浜会議センター、 2002 年 11 月

2. T. SOMEKAWA, C. YAMANAKA, M. FUJITA, M. C. D. GALVEZ, 「Five-Wavelength Polarization Backscattering Lidar Using a Coherent White Light Continuum」、『日本分光学会』、P57、 東京工業大学、 2005 年 5 月

3. 染川智弘、山中千博、藤田雅之、M. C. Galvez、「コヒーレント白色光を用いた偏光ライダー」、 『第 24 回レーザーセンシングシンポジウム』、P-5、鴨川グランドホテル、2005 年 9 月

4. 染川智弘、「コヒーレント白色光の多波長・偏光を利用した環境計測」、 『大阪大学 21 世紀 COE プログラム「究極と統合の新しい基礎科学」第 2 班「新物性の創成」若手夏の学校「超の世界にチャレンジ」』、PC-11、高野山福智院、2006 年 9 月

5. 染川智弘、「超広帯域コヒーレント光を用いた新しいリモートセンシング技術の開発」、 『大阪大学 21 世紀 COE プログラム「究極と統合の新しい基礎科学」若手秋の学校「普遍性と多様性の共存する 21 世紀の新しい基礎科学の芽」』、P2-39、蒜山高原休暇村、2007 年 10 月

Awards

1. 日本分光学会 平成 17 年度春季講演会 優秀発表賞
2. 21 世紀ＣＯＥプログラム「究極と統合の新しい基礎科学」平成 18 年 第 2 班・若手夏の学校 ポスター賞